Featured in Physics

Soft X-Ray Phase Nanomicroscopy of Micrometer-Thick Magnets

Jeffrey Neethirajan,[1,*] Benedikt J. Daurer,[2] Marisel Di Pietro Martínez,[1,3] Aleš Hrabec,[4,5] Luke Turnbull,[1,3]
Rikako Yamamoto,[1,3] Marina Raboni Ferreira,[6,7] Aleš Štefančič,[8] Daniel Alexander Mayoh,[8] Geetha Balakrishnan,[8]
Zhaowen Pei,[9] Pengfei Xue,[9] Liao Chang,[9] Emilie Ringe,[10,11] Richard Harrison,[11] Sergio Valencia,[12]
Majid Kazemian,[2] Burkhard Kaulich,[2] and Claire Donnelly[1,3,†]

[1]*Max Planck Institute for Chemical Physics of Solids, 01187 Dresden, Germany*
[2]*Diamond Light Source, Harwell Science and Innovation Campus, Didcot 0X11 ODE, United Kingdom*
[3]*International Institute for Sustainability with Knotted Chiral Meta Matter (WPI-SKCM^2),*
Hiroshima University, Hiroshima 739-8526, Japan
[4]*Laboratory for Mesoscopic Systems, Department of Materials, ETH Zurich, 8093 Zurich, Switzerland*
[5]*Laboratory for Multiscale Materials Experiments, Paul Scherrer Institute, 5232 Villigen PSI, Switzerland*
[6]*Brazilian Synchrotron Light Laboratory, Brazilian Center for Research in Energy and Materials,*
13085-970 Campinas, Brazil
[7]*Gleb Wataghin Institute of Physics, University of Campinas, 13083-859 Campinas, Brazil*
[8]*Department of Physics, University of Warwick, Coventry CV4 7AL, United Kingdom*
[9]*Laboratory of Orogenic Belts and Crustal Evolution, School of Earth and Space Sciences,*
Peking University, Beijing 100871, People's Republic of China
[10]*Department of Materials Science and Metallurgy, University of Cambridge,*
Cambridge CB2 3EQ, United Kingdom
[11]*Department of Earth Sciences, University of Cambridge, Cambridge CB2 3EQ, United Kingdom*
[12]*Helmholtz-Zentrum Berlin für Materialien und Energie, 12489 Berlin, Germany*

(Received 5 September 2023; revised 5 February 2024; accepted 31 May 2024; published 15 August 2024)

Imaging of nanoscale magnetic textures within extended material systems is of critical importance to both fundamental research and technological applications. While high-resolution magnetic imaging of thin nanoscale samples is well established with electron and soft x-ray microscopy, the extension to micrometer-thick systems currently requires hard x rays, which limits high-resolution imaging to rare-earth magnets. Here, we overcome this limitation by establishing soft x-ray magnetic imaging of micrometer-thick systems using the pre-edge phase x-ray magnetic circular dichroism signal, thus making possible the study of a wide range of magnetic materials. By performing dichroic spectroptychography, we demonstrate high spatial resolution imaging of magnetic samples up to 1.7 μm thick, an order of magnitude higher than conventionally possible with soft x-ray absorption-based techniques. We demonstrate the applicability of the technique by harnessing the pre-edge phase to image thick chiral helimagnets, and naturally occurring magnetite particles, gaining insight into their three-dimensional magnetic configuration. This new regime of magnetic imaging makes possible the study of extended non-rare-earth systems that have until now been inaccessible, including magnetic textures for future spintronic applications, non-rare-earth permanent magnets for energy harvesting, and the magnetic configuration of giant magnetofossils.

DOI: 10.1103/PhysRevX.14.031028

Subject Areas: Condensed Matter Physics, Magnetism, Materials Science

I. INTRODUCTION

Magnetic materials have a high impact on our society, with a range of functionalities making possible a number of applications. On one hand, the study of naturally occurring magnetite gives insight into magnetoreception [1] and the role of Earth's magnetic field over geological time [2]. On the other hand, strong magnetic fields from highly anisotropic permanent magnets play a key role in the production of clean energy [3–5], highly inductive magnets play an important role in write heads in hard disk drives [6], and

---

[*] Contact author: Jeffrey.Neethirajan@cpfs.mpg.de
[†] Contact author: Claire.Donnelly@cpfs.mpg.de

topological textures in spintronics devices promise the next generation of computing technologies [7,8].

Key to the behavior of these magnetic systems is their underlying magnetization configuration, which forms local areas of uniform magnetization—called magnetic domains—as well as nanoscale topological magnetization defects such as domain walls. Direct imaging of the magnetization configuration provides a unique insight into the underlying mechanisms responsible for their behavior. For example, imaging the reversal processes of permanent magnets elucidates their switching mechanisms [9], allowing for the development of more efficient devices, while imaging of the propagation of topological magnetization textures has led to devices based on the ultrafast motion of magnetic defects through interconnected networks [7,10] and nonlinear dynamics, enabling new types of computing architectures [11].

With such a diversity of magnetic systems, we require a broad range of capabilities to image the underlying magnetic configurations. First, we require the ability to study systems of varying dimensions, from single atoms to thick magnetic systems. Second, we require flexibility to study a wide variety of materials, from naturally forming magnetite to exotic designed topological and chiral magnets. Lastly, we require sufficient spatial resolution to resolve magnetic textures on the order of the magnetic exchange length: down to tens of nanometers and below, which corresponds to the typical sizes of key topological textures such as domain walls, skyrmions, and even hopfions.

However, while for thin samples (<300 nm) and surfaces, material flexibility and spatial resolution are well established with high spatial resolution soft x-ray [12,13] and electron microscopies [14,15], the imaging of thicker extended systems is more challenging. High spatial resolution imaging of extended samples of thicknesses on the order of hundreds of nanometers to micrometers has been achieved with resonant hard x-ray dichroic imaging [16] which, when combined with tomographic imaging, has revealed singularities known as Bloch points, skyrmions, and magnetic vortex rings [17–20] within micrometer-thick samples, with spatial resolutions down to 50 nm [19]. However, in the hard x-ray regime, x-ray dichroic signals are highly material dependent: While relatively strong signals exist for certain materials such as rare-earth-containing compounds, hard x-ray dichroic signals of transition metal magnets are approximately 20× weaker [16]. These significantly weaker dichroic signals result in poorer spatial resolution and imaging quality, thus generally limiting 3D investigations in these materials to thin films. When we schematically represent these existing capabilities for imaging samples of different thicknesses and compositions, as highlighted in red in Fig. 1, we identify a thickness gap corresponding to a range of material systems that remain inaccessible.

Here, we establish a route to the high spatial resolution magnetic imaging of extended magnetic systems that is applicable to a wide range of magnetic materials with soft x rays. By exploiting the phase XMCD signal, which is

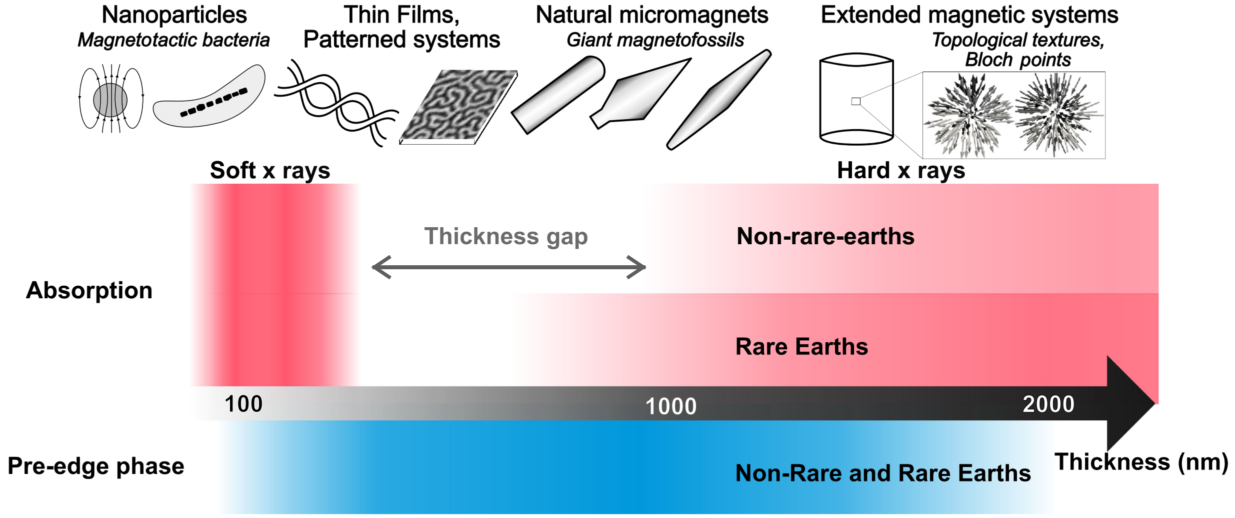

FIG. 1. Comparison of existing (red) magnetic nanomicroscopy capabilities for magnetic samples of different thicknesses with the capabilities of pre-edge phase x-ray magnetic circular dichroism (XMCD) contrast (blue). Absorption-based soft x-ray microscopy are limited to investigating the magnetic configuration of thin films and surfaces ($\lesssim$300 nm), whereas hard x-ray dichroic signals are highly material dependent and generally suitable for imaging systems $\gtrsim$1 μm. This opens a "thickness gap" in the range of samples that can be accessed, with the magnetic imaging of systems generally limited to "thin films" ($\lesssim$300 nm) or thicker, rare-earth containing samples ($\gtrsim$1 μm). The soft x-ray pre-edge phase XMCD (blue), that can be measured with coherent diffractive imaging (CDI) techniques fills this thickness gap, offering a route to measure magnetic samples of a variety of compositions up to micrometers in thickness.

prominent in the preabsorption edge, we extend soft x-ray magnetic imaging at transition metal edges to samples an order of magnitude thicker than currently viable, opening up a new regime for the imaging of magnetic compounds. We gain access to the phase contrast using x-ray ptychography, a CDI technique [21]. By performing dichroic spectroptychography, we map out the complex XMCD signal, revealing a notable phase XMCD signal in the preabsorption edge where the absorption contrast vanishes. This pre-edge phase signal makes it possible to measure thicker samples, and in this way we image the magnetic configuration of samples up to 1.7 μm in thickness: an order of magnitude higher than what is typically measured with soft x rays. This extension of our capabilities effectively bridges the thickness gap, as illustrated by the blue shaded region in Fig. 1. We demonstrate the applicability of the pre-edge phase XMCD by imaging two further classes of magnetic systems: First, we image the magnetic configuration of a 900-nm-thick patterned chiral helimagnet [22], opening the door to investigations of the magnetization structure within thick chiral helimagnets. Second, we demonstrate the imaging of thick naturally occurring magnetite particles with morphologies consistent with both biogenic (giant magnetofossils) and detrital origin, providing a route to experimentally investigating their magnetic configuration and gaining insights into their geological origin.

II. COMPLEX XMCD SPECTRUM WITH PTYCHOGRAPHY

The limitation of soft x-ray magnetic imaging to thin samples exists due to magnetic scattering being a resonant effect. Indeed, when a photon energy is tuned close to an absorption edge between a core level and a magnetically polarized valence band, the electronic transition between the two bands is dependent on the helicity of the incoming photon and the projection of the magnetization vector along the direction of propagation of x rays [23–25]. Experimentally, this leads to differences in absorption of the x rays which, when combined with nanomicroscopy, can provide projections of the magnetization in a sample. When compared to electron microscopy, which is limited to thin samples on the order of hundred nanometers in thickness, soft x rays provide a higher penetration depth while being element specific and directly probing the magnetization. However, for magnetic imaging, the localization of measurable XMCD signals to resonant energies, where the high absorption can lead to zero transmission for extended thick systems, has meant that both soft x rays and electron imaging have generally been limited to thin films on the order of hundreds of nanometers.

However, the magnetic contrast does not present itself only in the absorption: The scattering factor, and, therefore, the refractive index of a material, is complex, meaning that magnetic dichroism is also present in the phase of the transmitted wave (see Appendix A). With the development of lensless CDI techniques such as holography and ptychography, the full complex transmission function of an object becomes experimentally accessible with the help of phase retrieval algorithms [26]. These lensless imaging techniques have revolutionized x-ray imaging, with phase imaging of weakly absorbing objects [27,28] opening up the possibility to image biological samples [29] and the prospect of diffraction-limited spatial resolutions [30,31]. So far, magnetic imaging has mainly benefited from the high spatial resolutions that are available with lensless CDI techniques, bringing spatial resolutions down to 10 nm [30] and below [31]. However, although it has been seen that phase dichroism exists across the energy spectrum [16,29,32], offering possibilities for low radiation dose imaging [29,32], so far, magnetic phase imaging has not yet been fully exploited.

The x-ray phase dichroism is exploited here to extend the applicability of soft x-ray magnetic imaging to thicker systems. We first map the complex XMCD signal by imaging the magnetic configuration of a 100-nm-thick CoPt multilayer with perpendicular anisotropy. The multilayer film is grown by magnetron sputtering on an x-ray transparent silicon nitride membrane (see Appendix B). Subsequently, a hole of diameter approximately 3 μm in size is milled using a focused Ga ion beam to provide an empty region of the sample for image normalization and alignment. Dichroic spectroptychography is performed at the i08-1 beam line of the Diamond Light Source to map the complex XMCD signal from the magnetic domains in the sample. Specifically, circularly polarized x rays are microfocused onto the sample as it is scanned for several overlapping probe positions in the plane perpendicular to the direction of propagation of the x rays. For each position, a coherent diffraction pattern is collected in the far field by a two-dimensional detector. The complex transmission function of the object is then retrieved iteratively with the help of reconstruction algorithms [33,34]. A simple schematic of the experimental setup is shown in Fig. 2(a), and further experimental details are explained in Appendix C.

The reconstructed phase images taken using right circular polarized (RCP) and left circular polarized (LCP) x rays are shown in Fig. 2(b) and reveal a labyrinthlike domain structure in the CoPt film, with the magnetization in the domains oriented perpendicular to the sample plane and (anti)parallel to the direction of the propagation of the x rays. When the polarization is changed from RCP to LCP, the XMCD contrast reverses, allowing for the isolation of the magnetic signal as shown in Fig. 2(b). We define the amplitude XMCD (A_{XMCD}) and phase XMCD (ϕ_{XMCD}) signal as follows:

$$\begin{aligned} A_{\mathrm{XMCD}} &= \frac{\ln(A_{\mathrm{RCP}}) - \ln(A_{\mathrm{LCP}})}{2} \times 100, \\ \phi_{\mathrm{XMCD}} &= \frac{\phi_{\mathrm{RCP}} - \phi_{\mathrm{LCP}}}{2}, \end{aligned} \tag{1}$$

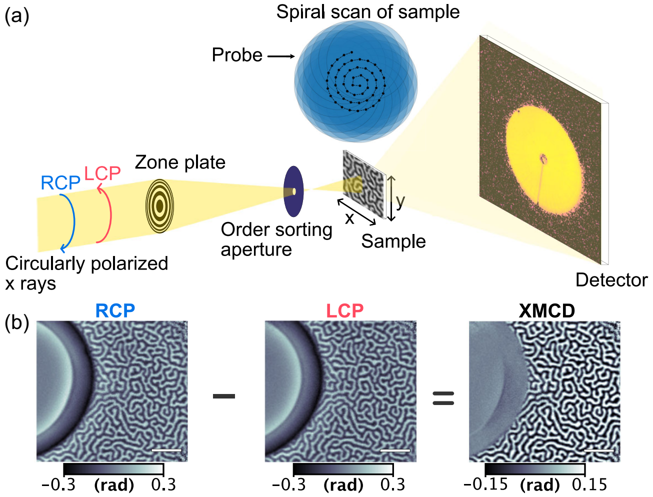

FIG. 2. (a) Schematic of the ptychography setup. The sample is scanned in the plane perpendicular to the direction of propagation of the x rays, for overlapping probe illumination positions, as indicated in the inset. Diffraction patterns are measured in the far field. (b) Ptychographic phase projections measured with RCP and LCP x rays, with the difference giving the XMCD signal, indicating the projection of the magnetization (anti)parallel to the x-ray beam. The semicircle is a hole milled using a focused Ga ion beam which provides an empty region of the sample for image normalization and alignment. The scale bar represents 1 μm.

where A_{RCP}, A_{LCP}, ϕ_{RCP}, and ϕ_{LCP} are the amplitude and phase projections taken with RCP and LCP x rays, respectively. In order to map the complex XMCD signal across the L_3 and L_2 edges, dichroic spectroptychography scans are performed for a range of energies between 770 and 807 eV in the vicinity of the Co L_3 and L_2 absorption edges with RCP and LCP x rays. The dichroic A_{XMCD} and ϕ_{XMCD} images for a select few energies are given in Fig. 3(a). To extract the complex XMCD signal, the domains are segmented and their contrast averaged (details explained in Appendix D) to obtain the quantitative spectra plotted in Fig. 3(b). The solid black curve, shown in Fig. 3(b), represents the transmission spectrum through the sample, providing a direct comparison between the strength of the respective XMCD signals and transmission through the sample. We first consider the A_{XMCD}, with the images highlighted by the red dotted box in the top row in Fig. 3(a), and the extracted A_{XMCD} spectrum given by the red curve in Fig. 3(b). Two resonance peaks of opposite sign can be observed across the L_3 and L_2 edges, where domain contrast reversal can also be seen in the A_{XMCD} images. The signal and the domain contrast is strongest at the energy associated with highest absorption (780 eV), and already drops to zero, 1.8 eV below the L_3 resonance peak, with the magnetic domains no longer resolvable in the images.

We next consider the ϕ_{XMCD} signal, represented by the blue curve in Fig. 3(b). Corresponding domain contrast can be observed in almost all of the ϕ_{XMCD} projections at different energies, highlighted by a blue dotted box in Fig. 3(a). The ϕ_{XMCD} signal is particularly strong in the vicinity of the L_3 and L_2 edges, with the maximum occurring 0.5 eV below the L_3 absorption edge and with images showing strong contrast around 779.4 and 794.4 eV. In the preabsorption edge, the ϕ_{XMCD} domain contrast is opposite to A_{XMCD}, while we observe a ϕ_{XMCD} contrast reversal across the two absorption edges. Most notably, the difference between the ϕ_{XMCD} and A_{XMCD} is that, while the A_{XMCD} is restricted to on-resonance energies, the ϕ_{XMCD} signal is nonzero across almost all energies measured, specifically in the preabsorption edge where the magnetic domains can even be resolved 10 eV below the absorption edge, where the transmission through the sample is significantly higher. To visualize this difference in the energy-dependent measurable contrast, we have shaded the regions of the spectrum in Fig. 3(b), where red regions indicate the energies for which the A_{XMCD} is measurable (as well as the ϕ_{XMCD}), while blue regions indicate the energy regime for which only the ϕ_{XMCD} is detectable. The ϕ_{XMCD} is available for a much wider range of available energies than the A_{XMCD}, offering a more flexible contrast mechanism.

III. MODELLING THE IMAGING OF MICROMETER-THICK MAGNETIC SYSTEMS

The importance of the flexibility of the contrast mechanism becomes clear when we consider thicker systems. While on-resonance imaging with A_{XMCD} contrast works well for thin samples, as we increase the thickness above a threshold at which there is not sufficient transmission on-resonance for measurements, we will be forced to image off-resonance at energies associated with lower absorption. We explore this by calculating the transmission for thicker samples using the experimentally measured transmission spectrum of the CoPt multilayer and further calculating the complex XMCD signal (see Appendix E 1). We first consider the calculated transmission for thicker samples, shown in Fig. 4(a), with each row in the image representing transmission as a function of energy for a sample of a certain thickness. The darker regions indicate a lower transmission through the sample, and we observe a reduction in energies with significant transmission as the thickness increases. Examples of transmission spectra corresponding to selected thicknesses [indicated as colored lines on Fig. 4(a)] are given in Fig. 4(b), where one can observe a drop to zero transmission on-resonance for higher thicknesses.

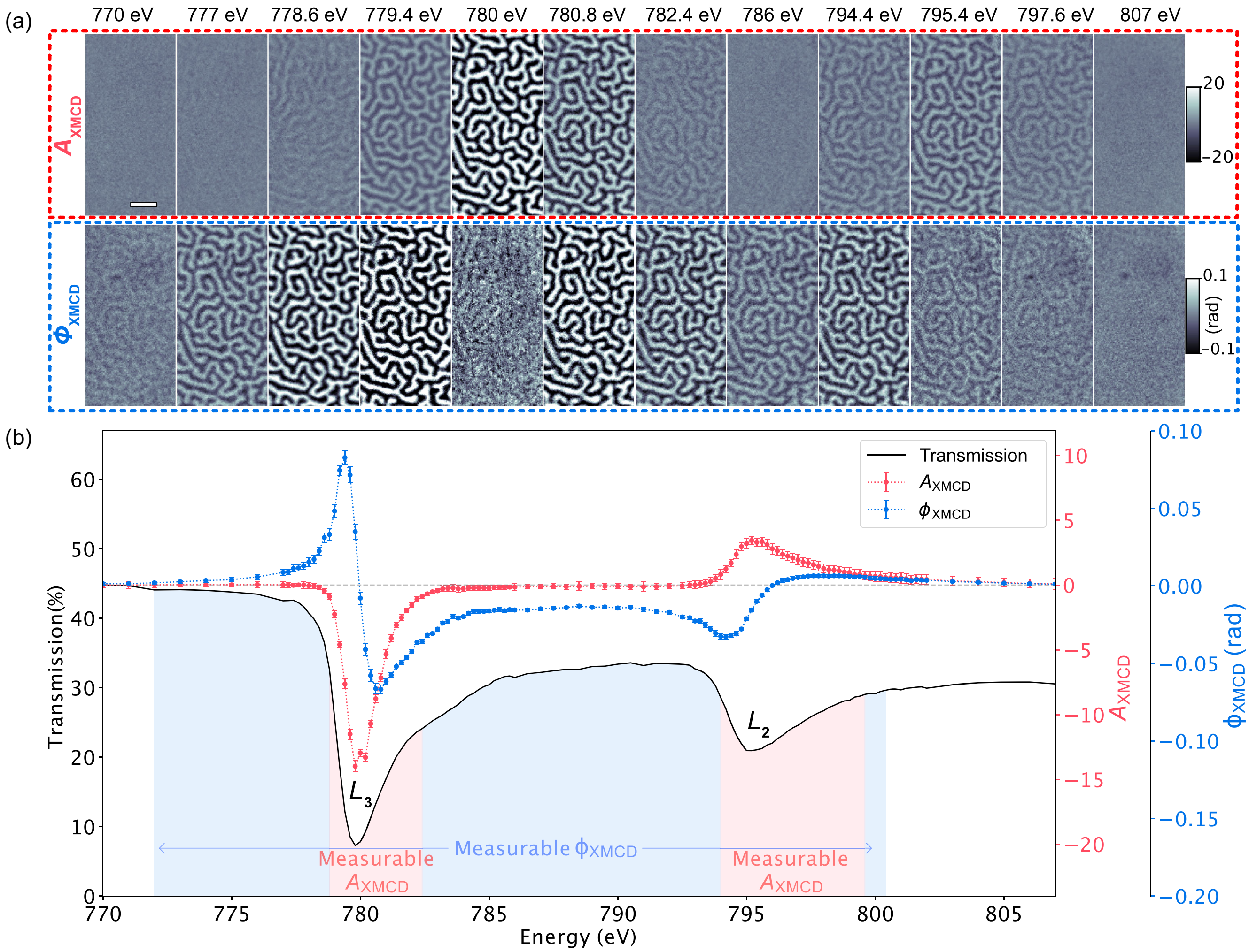

FIG. 3. Dichroic spectroptychography across the Co L_3 and L_2 absorption edges of a 100-nm-thick CoPt multilayer system. (a) The amplitude (A_{XMCD}) and phase (ϕ_{XMCD}) XMCD images across a selected range of energies. The scale bar represents 500 nm. (b) A_{XMCD} (red) and ϕ_{XMCD} (blue) XMCD spectra across the Co $L_{2,3}$ edges extracted from domains seen in the XMCD images plotted in (a). The black curve represents the transmission through the thickness of the sample. The ϕ_{XMCD} spectra exhibit a nonzero signal throughout the entire range of energy except on-resonance. The A_{XMCD} signal is notably strong only on-resonance, when transmission is minimum, and vanishes at energies 1.8 eV below the L_3 absorption edge. The blue shaded region represents areas where only ϕ_{XMCD} is measurable, and red shaded regions represent areas where A_{XMCD} is also measurable.

We next consider the complex XMCD signal for thicker samples, by plotting the energy at which both strongest A_{XMCD} and ϕ_{XMCD} signals can be extracted for increasing thickness in Fig. 4(c). We observe that above a threshold thickness, indicated by the dashed line in Fig. 4(c), the optimal energy at which the XMCD can be measured drops steadily. This decrease in the measurement energy, to energies associated with higher transmission, has further implications when we consider the dependence of the A_{XMCD} and ϕ_{XMCD} signal on the energy-dependent transmission. Indeed, by plotting the complex pre-edge XMCD signal, measured for 100 nm CoPt shown in Fig. 3(b), as a function of transmission in Fig. 4(d), we observe a significant difference: The A_{XMCD} is maximum for energies corresponding to lower transmission and decays exponentially as the transmission is increased. In contrast, the ϕ_{XMCD} signal is maximum for energies corresponding to higher transmission and decays linearly as the transmission is increased, thus exhibiting a weaker dependence on the transmission of the sample. For purely absorption-based imaging, the requirement to measure at lower off-resonance energies, thus, quickly leads to the suppression of the XMCD signal; however, access to the pre-edge ϕ_{XMCD} opens the possibility to measure thicker samples.

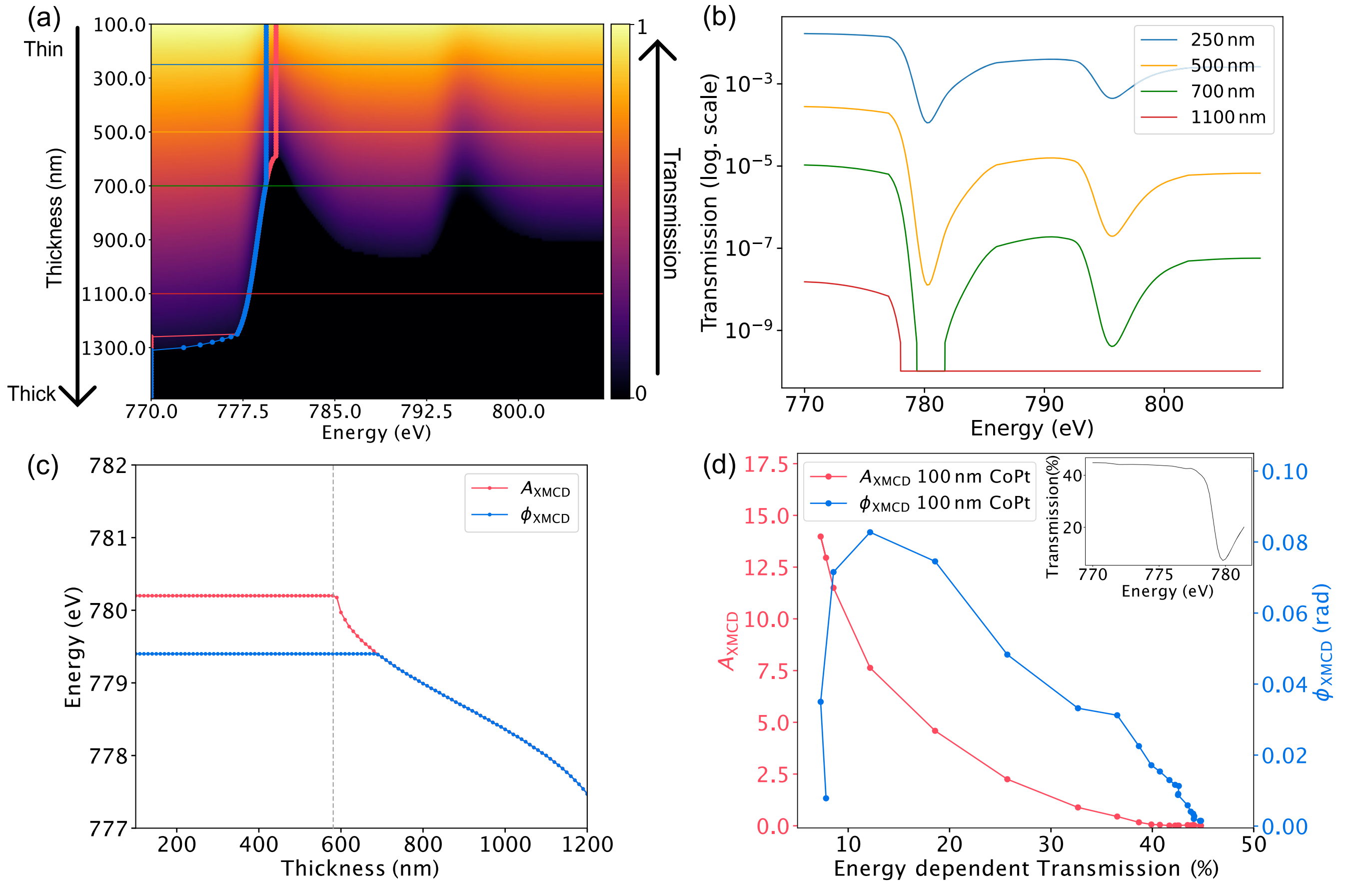

FIG. 4. (a) Calculated transmission of thicker CoPt films as a function of energy across the Co L_3 and L_2 absorption edges. The darker regions indicate regions of low or zero transmission. As the thickness is increased, we are forced to measure at preabsorption edge energies where transmission is significantly higher than on-resonance, indicated by the red and blue dotted lines for A_{XMCD} and ϕ_{XMCD}, respectively. (b) Transmission spectra for a few select calculated thicknesses taken across the line corresponding to the lines shown in (a). (c) Optimal energies at which strongest A_{XMCD} and ϕ_{XMCD} can be extracted as sample thickness is increased. (d) Evolution of the complex pre-edge XMCD signal as a function of transmission which varies as a function of the energy of the incident photon as shown in the inset. As one moves to energies corresponding to higher transmission, A_{XMCD} exhibits an exponential decay, while the ϕ_{XMCD} exhibits a linear decay.

To explore the evolution of the A_{XMCD} and ϕ_{XMCD} for increasing thickness, we investigate the dimensionless signal to noise ratio (SNR) for the calculated A_{XMCD} and ϕ_{XMCD} as a function of effective thickness (scaled for comparison with experimental data, see Appendix E), plotted in Fig. 5(b) (dashed lines). For thinner samples, where the A_{XMCD} SNR is significantly higher than the ϕ_{XMCD} SNR, the A_{XMCD} SNR peaks at a thickness corresponding to the suppression of on-resonance transmission and decreases exponentially afterward. However, the ϕ_{XMCD} SNR increases at a slower rate, peaking at a higher effective thickness but retaining a high SNR to yet higher thicknesses. We identify a thin regime, where the A_{XMCD} SNR provides a significantly better image quality, and a thick regime, where ϕ_{XMCD} SNR provides higher-quality images.

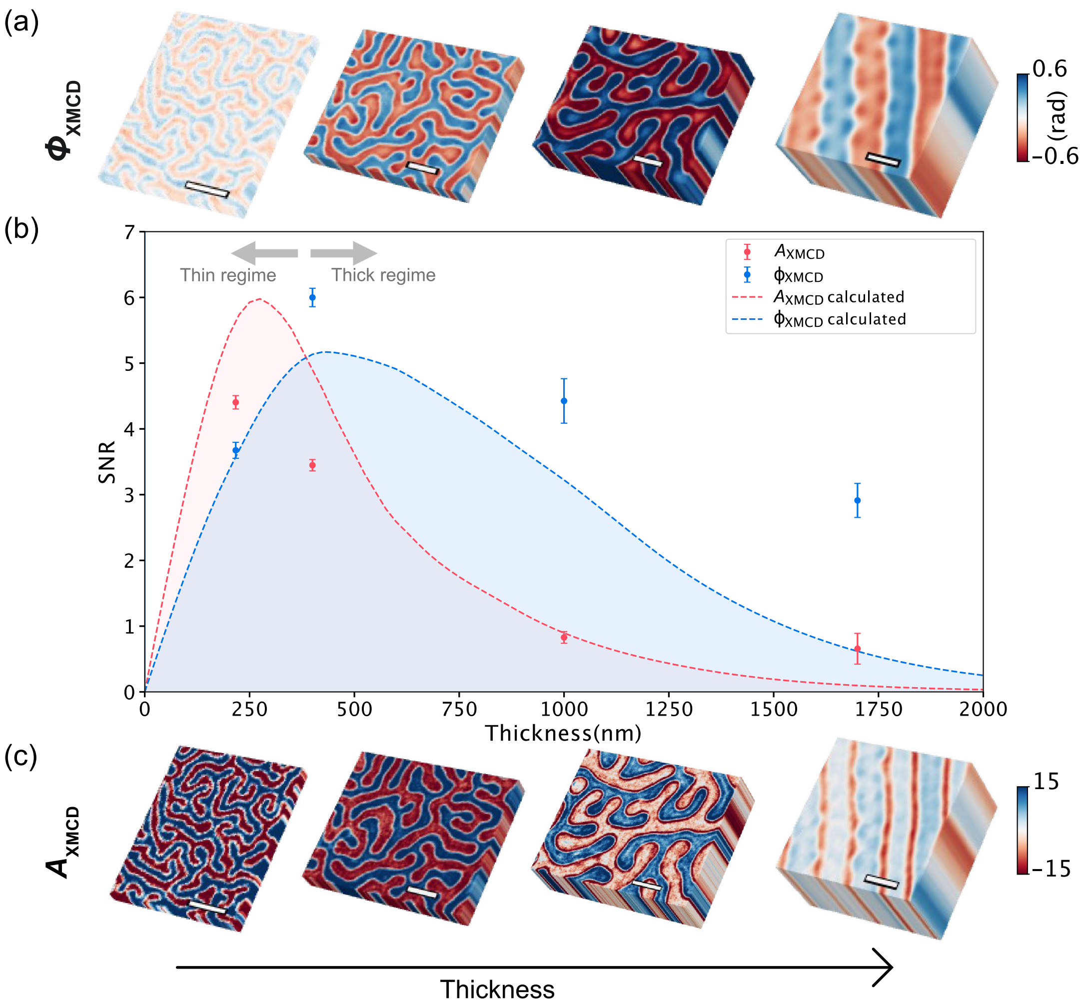

FIG. 5. (a),(c) ϕ_{XMCD} and A_{XMCD} imaging of magnetic films of increasing thickness. The XMCD projections with highest SNR of the 100-nm-thick CoPt are measured at 780 and 779.4 eV for A_{XMCD} and ϕ_{XMCD}, respectively. The XMCD projections with highest SNR for the 400 nm, 1 μm, and 1.7 μm FeGd films are measured at 709, 708.5, and 708 eV, respectively, for both A_{XMCD} and ϕ_{XMCD}. (b) Calculated highest SNR of A_{XMCD} and ϕ_{XMCD} for a range of thicknesses indicated by the red and blue dashed line, respectively. Note that the calculated thickness dependence of the CoPt XMCD SNR is scaled in thickness to allow for a comparison between the experimentally measured CoPt/FeGd data shown as red and blue dots (see Appendix E 3). We identify a "thin" regime, where the A_{XMCD} SNR provides a significantly better image quality, and a "thick" regime, where due to the pre-edge ϕ_{XMCD} we obtain high-quality projections for thick samples with high SNR. The highest A_{XMCD} and ϕ_{XMCD} SNR across the Co $L_{2,3}$ edges for 100-nm-thick CoPt (scaled to an effective thickness of 217 nm FeGd, see Appendix E 3) and 400 nm, 1 μm, and 1.7 μm FeGd. The extracted optimal SNR values from each of these XMCD projections is plotted, with red circular dots indicating the A_{XMCD} SNR and blue squares indicating the ϕ_{XMCD} SNR for the different thicknesses. The images shown in (a) and (c) are the projections from which the A_{XMCD} and ϕ_{XMCD} signal are extracted. The scale bar in the images represents 500 nm.

IV. IMAGING MAGNETIC STRIPE DOMAINS IN MICROMETER-THICK FILMS

We experimentally confirm this ability to image the magnetic state of thicker samples with high SNR ϕ_{XMCD} imaging by performing dichroic spectroptychography scans on FeGd films grown by magnetron cosputtering of thicknesses 400 nm, 1 μm, and 1.7 μm across the L_3 and L_2 edges of Fe (see Appendixes B and F). We first plot the highest SNR images for ϕ_{XMCD} and A_{XMCD} in Figs. 5(a) and 5(c), respectively, where it can be seen that the quality of the images is highly thickness dependent and that this thickness dependence is different for the two contrast mechanisms. In particular, for the A_{XMCD}, the quality of the image appears to decrease steadily with thickness, with a loss of quantitative XMCD signal for thicknesses of 1 μm and above, with contrast present only in the vicinity of the domain walls. For the ϕ_{XMCD}, the maximum quality instead appears to occur at 1 μm, and the quantitative measurement of the magnetic domain structure (indicated by the equal and opposite magnetic contrast in positive and negative domains) is retained for all sample thicknesses. Because of the strong perpendicular anisotropy, it is assumed that the magnetization in the domains is aligned parallel or antiparallel to the x-ray beam and that changes in contrast are due to the thickness dependence of the XMCD signal (see Appendixes A and E). Furthermore, the ϕ_{XMCD} images have a higher spatial resolution than the A_{XMCD} images for samples in the thick regime, see Appendix G. For tomographic imaging, the maximum thickness of the sample that can be measured is limited by the increase in effective thickness as the sample is tilted. In this context, the combination of pre-edge phase imaging with tomography provides an opportunity to extend the capabilities of 3D imaging to thicker systems, albeit with a slightly reduced maximum thickness than can be achieved for 2D imaging.

To quantitatively compare both A_{XMCD} and ϕ_{XMCD} for the various thicknesses in these images, we calculate the SNR of the measured A_{XMCD} and ϕ_{XMCD} projections, combining our 100 nm CoPt and thicker FeGd films by defining an effective thickness (see Appendix E 3). The SNR of the images is plotted as a function of effective thickness in Fig. 5(b), with red and blue dots representing the measured A_{XMCD} and ϕ_{XMCD} SNR, respectively. As observed in the images, we see a clear difference in the thickness dependence, with the ϕ_{XMCD} providing higher SNR imaging of magnetic domains for thicknesses up to 1.7 μm, the thickest film that is measured.

By comparing with our calculated SNR plotted in Fig. 5(b) (dashed lines), it can be seen that the ϕ_{XMCD} imaging can extend to samples up to 2 μm, an order of magnitude thicker than what is currently achievable with soft x-ray absorption imaging. While this exact thickness dependence is highly material dependent, this new approach addresses a key limitation of current imaging capabilities, making possible the high spatial resolution mapping of thicker transition metal-based systems that until now have been inaccessible. We note that the experimental and calculated values originate from FeGd and CoPt samples, respectively. Because of the different absorption coefficients of the materials, there are, therefore, differences in the quantitative values of the calculated and experimental data. However, the general trend of the A_{XMCD} and ϕ_{XMCD} matches well.

V. IMAGING THE MAGNETIC CONFIGURATION OF THICK HELIMAGNETS

We demonstrate the applicability of our technique beyond our model stripe domains to a wider range of systems by applying the pre-edge ϕ_{XMCD} contrast imaging to thick helimagnets. Helimagnets are magnetic materials that, due to the broken inversion symmetry of the crystal lattice, are intrinsically chiral, giving rise to an antisymmetric Dzyaloshinskii-Moriya interaction (DMI). The resulting interplay between the ferromagnetic exchange interaction, DMI, and external fields results in the formation of complex topological textures such as skyrmions [35,36], chiral bobbers [37], and hopfions [38–41].

Here, we demonstrate the imaging of a patterned single-crystal lamella of $\mathrm{Co_8Zn_9Mn_3}$ that is 900 nm thick (see Appendix B). To determine the effectiveness of the pre-edge ϕ_{XMCD}, we perform dichroic ptychography at the Co L_3 edge. As there is no transmission on-resonance, we tune the energy 3 eV below the Co L_3 edge at 777 eV, in order to maximize the measured XMCD contrast and recover transmission through the sample. A phase electronic projection (ϕ_{Elec}) is given in Fig. 6(a), showing a narrow bridgelike region of width approximately 400 nm and a larger cylindrical region about 1.4 μm in diameter. A comparison between the measured A_{XMCD} and ϕ_{XMCD} projections is given in Figs. 6(b) and 6(c), respectively, where one can observe white and black stripes corresponding to the helical winding of the magnetization, as expected for a zero field magnetic configuration [42]. Although magnetic contrast is seen for both A_{XMCD} and ϕ_{XMCD}, the quality of the XMCD signal in the ϕ_{XMCD} is significantly higher, revealing details that cannot be seen in the A_{XMCD} images. Specifically, in the narrow bridgelike region, the helical stripes are relatively clear and ordered, while within the larger cylindrical region, the contrast of the helices is nonuniform, suggesting a difference in the 3D magnetization configuration between the two regions.

We gain insight into the 3D magnetization configuration of the thick helimagnet by measuring a second set of dichroic ptychographic projections with the sample tilted by −44° about the Y axis of the sample plane, increasing the effective sample thickness to 1.25 μm along the direction of x-ray propagation. The ϕ_{Elec} projection of the sample at this tilted geometry is shown in Fig. 6(d), while the A_{XMCD} and ϕ_{XMCD} projections are shown in Figs. 6(e) and 6(f), respectively. In this tilted configuration, the ϕ_{XMCD} again provides higher SNR images ($\mathrm{SNR} = 4.74$) than the A_{XMCD} ($\mathrm{SNR} = 0.27$). This difference in the SNR can be seen clearly when we plot line profiles taken across the center of the projection of the tilted sample, shown in Figs. 6(g) and 6(h) for A_{XMCD} and ϕ_{XMCD}, respectively. The A_{XMCD} profile is dominated by noise, whereas the ϕ_{XMCD} exhibits a clear oscillating signal with an average period of 125 nm that corresponds to the expected wavelength of the helical stripes [42].

Considering the ϕ_{XMCD} projections at 0° and −44° provides insight into the 3D magnetization configuration of the helical stripes and the role of confinement in the different regions of the sample. We first consider the bridgelike region: While at 0° the projection shows strong stripe contrast, at −44° the XMCD contrast becomes significantly weaker uniformly across the region, consistent with a uniform ordering of the helices through the thickness of the sample. In contrast, in the unconfined cylindrical region of the sample, the helical contrast becomes weak or vanishes at different points in the normal and tilted projections, indicating nonuniform ordering of the helices through the thickness of the sample. For example, in the edge [indicated by the orange arrow in Figs. 6(e) and 6(f)],

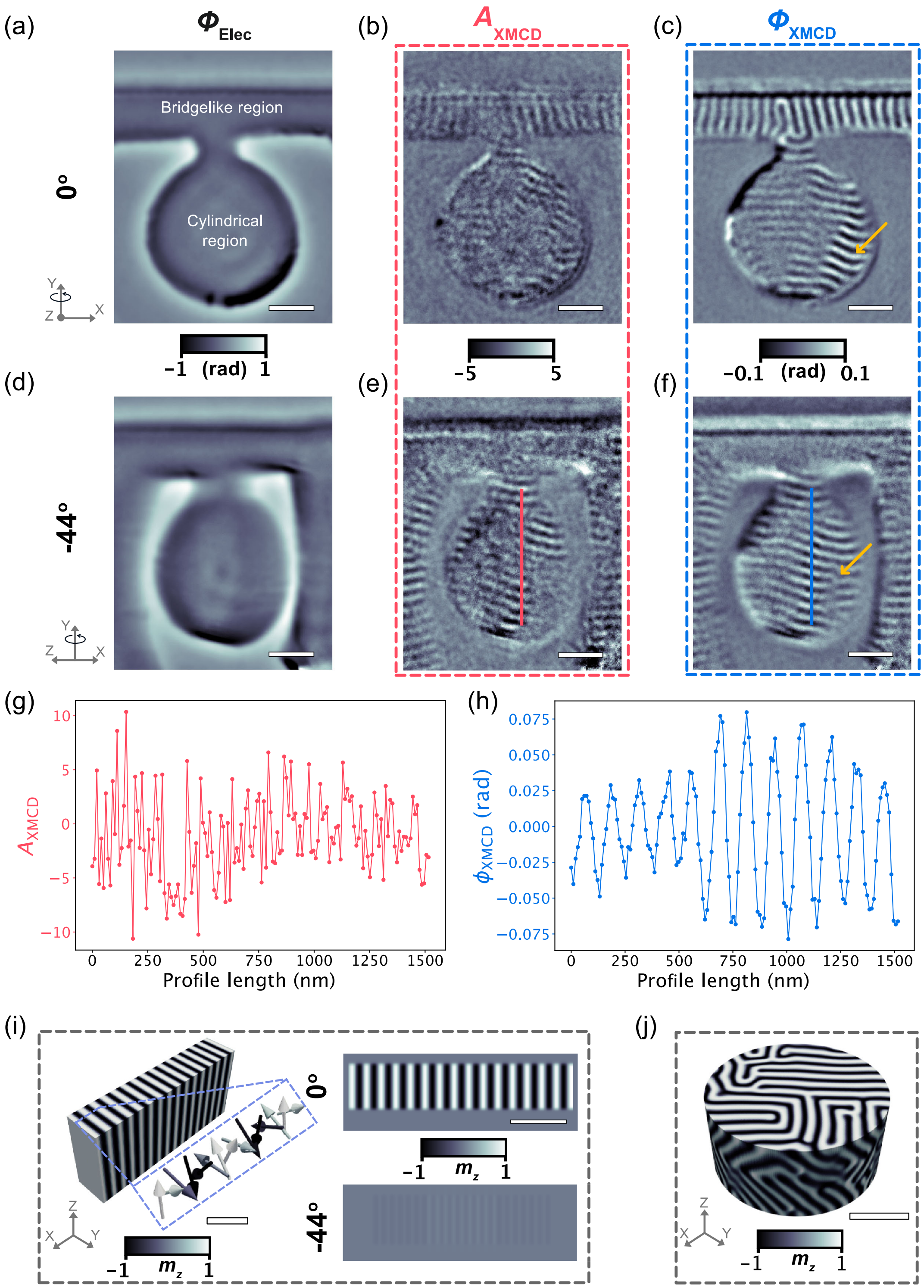

FIG. 6. Pre-edge phase imaging of $Co_8Zn_9Mn_3$ helimagnet at 777 eV at the Co L_3 pre-edge. (a)–(c) Electronic (ϕ_{Elec}), A_{XMCD}, and ϕ_{XMCD} projections of the 900-nm-thick helimagnetic sample taken with x rays at normal incidence (0°). (d)–(f) Electronic (ϕ_{Elec}), A_{XMCD}, and ϕ_{XMCD} projections of the sample tilted by $-44°$ about the Y axis of the sample plane. The magnetic contrast reveals helical stripes. Comparison between the A_{XMCD} and ϕ_{XMCD} image taken in the pre-edge at normal incidence and at a tilted angle of $-44°$ reveals that ϕ_{XMCD} images have a much higher SNR and provide a clearer magnetic contrast. (g),(h) Line profiles taken across the center of the sample as denoted by the red and blue lines in (e) and (f), respectively. The A_{XMCD} profile is very noisy with low SNR, whereas the ϕ_{XMCD} profile exhibits a clear oscillating signal with a periodicity of 125 nm corresponding to the wavelength of the helical stripes. (i) Simulation of the confined region of the sample shows the formation of elongated vertical helices. The projection along the thickness of the elongated helices at 0° exhibits strong stripe contrast, whereas the projection at $-44°$ shows a weaker contrast as the stripes overlap and cancel. (j) Simulation of an unconfined region with similar dimensions as the cylindrical region in the patterned sample in (a)–(f) exhibits a more complex 3D ordering of the magnetization configuration. The scale bar in the images represents 500 nm.

strong XMCD contrast is observed at 0° where a reorientation of the helical stripes is seen. When the same region is considered at −44°, one can identify that the reorientation is associated with the presence of dislocations between two helical domains. This is consistent with a complex three-dimensional helical ordering. The difference in magnetic configuration between the bridgelike and cylindrical regions indicates that the helical state is strongly influenced by confinement. Indeed, when we perform micromagnetic simulations of a bridge and cylinder of similar dimensions as our patterned sample (see Appendix H), shown in Figs. 6(i) and 6(j), we can reproduce this difference: In the bridge, the helices form elongated stripes perpendicular to the long axis, while in the cylinder, the state is more disordered, with no preferential orientation of the stripes. Considering XMCD projections of the micromagnetic simulations, for the narrower bridge, the XMCD contrast is strong at 0° and becomes much weaker at −44° due to the elongated helical stripes overlapping and canceling out, consistent with the ϕ_{XMCD} projections in Figs. 6(c) and 6(f). The difference between these two regions highlights the role of confinement in the 3D helical ordering: For a thick patterned sample of approximately 400 nm in width, the lateral confinement strongly influences the magnetic configuration. In the patterned cylinder of diameter 1.4 μm, for which the thickness of 900 nm (7.5× the winding length of the helimagnet) is the smallest length scale, the role of confinement is strongly reduced, allowing for the formation of more complex magnetic configurations. These results indicate that the threshold for the transition between a strongly confined, ordered state and an unconfined disordered state lies between the length scales of 400 and 900 nm (equivalently, between 3.3× and 7.5× the winding length of the helimagnet), a regime that is now made accessible with pre-edge XMCD imaging. The ability to image such thick helimagnet systems with the pre-edge ϕ_{XMCD} opens the door to the study of unconfined chiral configurations. This insight into the role of geometry and varying degrees of confinement in the ordering of helimagnets is particularly significant due to the recent discovery of hopfions, which, alongside textures such as skyrmion braids, show complex ordering through the thickness of such systems. In combination with 3D magnetic vector imaging [13,17,19,43–46], we envisage that the pre-edge ϕ_{XMCD} will be vital in mapping these 3D chiral textures in real space.

VI. IMAGING THE MAGNETIC CONFIGURATION OF THICK MAGNETITE PARTICLES

We further demonstrate the utility of pre-edge ϕ_{XMCD} imaging on a selection of naturally occurring magnetite particles that were collected from marine sediments linked to historical warming periods [47]. The particles exhibit distinct morphologies of unknown origin and are

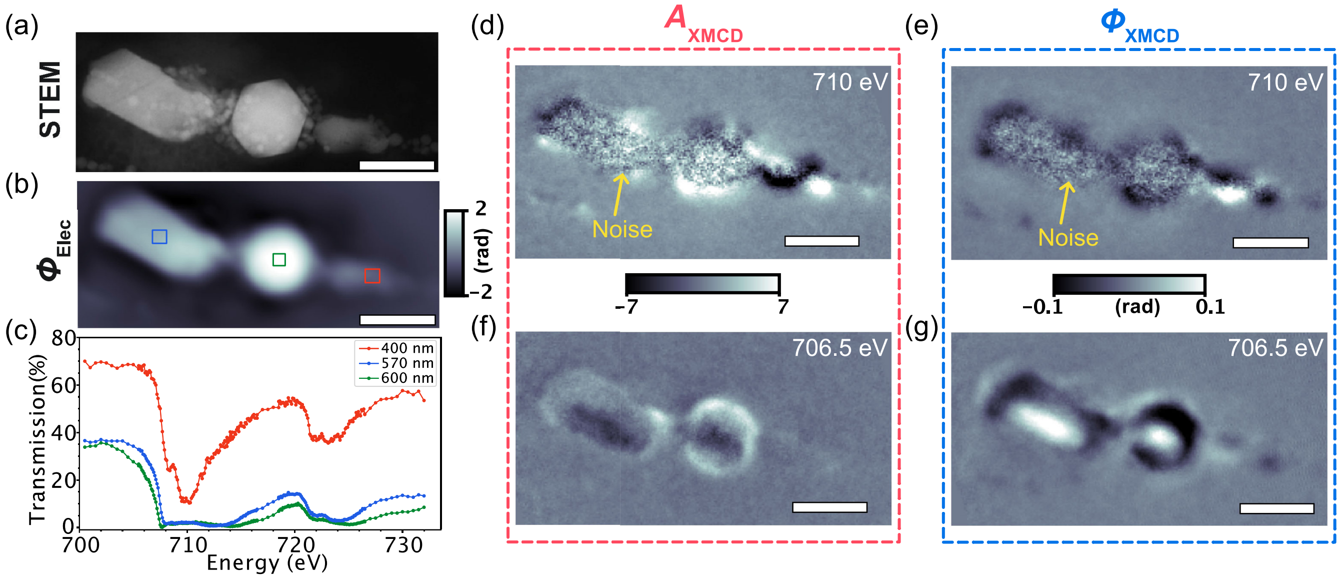

FIG. 7. Pre-edge phase imaging of naturally occurring magnetite particles. (a) STEM image of three magnetite particles of different size and morphologies. (b) Electronic phase projection (ϕ_{Elec}) obtained with pre-edge x-ray ptychography taken with x rays at normal incidence (0°). (c) Transmission spectra of the different particles of different thicknesses, where one can see that the thin particle [red line, red box in (b)] transmits at all energies, whereas the transmission goes to zero on-resonance for the thicker particles [green, blue lines and boxes in (b)]. (d) A_{XMCD} and (e) ϕ_{XMCD} projections of the magnetite particles on-resonance, where XMCD signal is measurable in the thin region and only noise is measured in the nontransmitting thick regions. (f) A_{XMCD} and (g) ϕ_{XMCD} projections of the magnetite particles in the pre-edge, where XMCD signal is measurable in all regions, with significantly higher signal to noise in the ϕ_{XMCD} projection. The scale bar in images represents 500 nm.

unknown origin and indicate a possible link between ancient events and the biomineralization of large magnetite crystals. A collection of such particles can be seen in the scanning transmission electron microscope (STEM) in Fig. 7(a) (see Appendix B). In particular, there is a thin structure around 400 nm thick, as well as a thicker bulletlike particle around 570 nm thick consistent with morphologies of certain giant magnetofossils [48]. In addition, the central particle exhibits a cuboctahedral structure around 600 nm thick that is likely of detrital rather than biogenic origin [48]. Previous attempts to image the magnetic state of unrelated particles with similar size and shape to this one have been made using high-acceleration-voltage electron holography [49]. However, this method still required samples to be sectioned into thinner pieces, resulting in a change to their natural magnetic state. Here, we demonstrate that, with pre-edge ϕ_{XMCD} soft x-ray imaging, we are able to image the entire particle nondestructively, thereby preserving (in principle) its natural magnetic state.

A ϕ_{Elec} projection acquired with ptychography is presented in Fig. 7(b), where one can resolve the three distinct particles. We perform spectroptychography and extract the transmission spectrum of each particle across the Fe L_3 and L_2 absorption edges, as presented in Fig. 7(c). We observe no saturation of transmission for the thin particle at all energies (red). However, the thicker bulletlike particle (green) and cuboctahedral-like particle (blue) do not transmit on-resonance. This is reflected in the on-resonance A_{XMCD} and ϕ_{XMCD} images presented in Figs. 7(d) and 7(e), where XMCD contrast can be seen for the thin region but only noise is observed in the thick regions, highlighted by the yellow arrows in Figs. 7(d) and 7(e). In contrast, when we measure in the pre-edge, 3.5 eV below resonance, XMCD contrast in all three particles can be measured. Again, as for the stripe domains and the helimagnets, the ϕ_{XMCD} provides significantly higher SNR of 7.5 than the A_{XMCD} SNR of 2.7, providing insight into the vortexlike magnetic configuration of the particles.

The ability to image the magnetic state of micron-sized magnetite particles opens the door to nondestructive investigation of naturally occurring magnetic mineral grains that lie between the single-domain (<100 nm) and multidomain (≫1000 nm) size thresholds. These intermediate-sized particles are now widely recognized as the dominant carriers of stable paleomagnetic signals in many geological materials [50,51] but are relatively poorly understood due to the complex nature of the vortex to multivortex states they contain. Our imaging method has the potential to reveal fundamental new insights into the magnetic state and behavior of such particles, with applications to a whole host of scientific questions, from the origin and purpose of giant magnetofossils to the history of magnetic fields in the solar nebula [49].

VII. CONCLUSION

In conclusion, we have demonstrated the soft x-ray magnetic imaging of thick magnetic systems with the pre-edge ϕ_{XMCD} signal. By determining the complex XMCD spectrum of a CoPt thin film across the L_3 and L_2 absorption edges of Co, we were able to not only identify the presence of a significant ϕ_{XMCD} signal in the pre-edge regime, but, by extrapolating these data, also to establish a new imaging regime where the ϕ_{XMCD} signal enables quantitative imaging of thick samples with high SNR and spatial resolution that would not be possible with traditional absorption-based techniques. Remarkably, our analysis predicts an order of magnitude increase in the accessible thickness regime due to the phase imaging, which we confirmed by imaging magnetic domains in FeGd samples of up to 1.7 μm in thickness. Beyond model systems, we apply this technique to two classes of materials. First, we image the magnetization of a patterned chiral helimagnet with an effective thickness of 1.25 μm, opening the door to 3D investigations of topological textures in micrometer-thick chiral magnets. Second, we demonstrate the imaging of naturally occurring thick magnetite particles, establishing a route to image the magnetic configuration of asteroid particles and giant magnetofossil particles.

One of the key advantages of pre-edge ϕ_{XMCD} imaging is that it is not limited to ptychography but can be exploited with any coherent imaging technique such as holography [29,46], allowing for complex sample environments including the application of fields or currents and cryogenic environments, as well as time-resolved studies. Moreover, by combining it with 3D imaging geometries [17,19,43,45,52], the pre-edge ϕ_{XMCD} offers a route to uncovering three-dimensional buried magnetization configurations in thicker samples of varying composition [46].

We expect pre-edge ϕ_{XMCD} imaging to have a significant impact on the field of magnetism, making possible the imaging of topological defects in higher-dimensional chiral magnets, where this newfound flexibility in the material and sample geometry will drive forward the discovery of exotic textures. Moreover, having demonstrated that it enables the nondestructive investigation of naturally occurring magnetic systems, it can be used to obtain insight into the formation and role of magnetofossils [53] and meteorites [54]. Finally, an immediate societal impact will be found with the study of materials critical to efficient and clean energy production, opening the door to the mapping of the internal configuration of non-rare-earth magnets [55].

Data and codes associated with this work are available at [56].

ACKNOWLEDGMENTS

Diamond Light Source provided access to the I08-1 Soft X-ray Ptychography Facility with experiment Grants No. MG28255-1, No. MG32635-1, No. MG32984-2, and No. MG33254-1. J. N., M. D. P. M., L. T., and C. D.

acknowledge funding from the Max Planck Society Lise Meitner Excellence Program and funding from the European Research Council (ERC) under the ERC Starting Grant No. 3DNANOQUANT 101116043. J. N. acknowledges support from the International Max Planck Research School for Chemistry and Physics of Quantum Materials. A. S., D. A. M., and G. B. thank Engineering and Physical Sciences Research Council United Kingdom for funding through Grants No. EP/T005963/1 and No. EP/N032128/1. This project has received funding from the European Union's Horizon 2020 research and innovation program under Grant Agreement No. 101005611. R. H. acknowledges funding by the Electron and X-ray microscopy Community for structural and chemical Imaging Techniques for Earth materials (EXCITE) (Award No. G106564). The authors thank Po-Yen Tung and Simone Finizio for fruitful discussions. Z. P., E. R., and R. H. acknowledge Thermo Fisher Scientific for providing access to and supporting the cryo-EM facilities at the Cambridge Pharmaceutical Consortium.

APPENDIX A: COMPLEX X-RAY MAGNETIC CIRCULAR DICHROISM

The complex reconstructed images obtained by ptychography can be expressed as $A(E)e^{i\phi(E)}$, where both amplitude (A) and phase (ϕ) are both highly energy dependent and embed information about the complex scattering factor given by

$$f(E, r) = \underbrace{f_c(E)[(\boldsymbol{\varepsilon}_f^* \cdot \boldsymbol{\varepsilon}_i)]}_{\text{Electronic}} - \underbrace{if_1(E)[(\boldsymbol{\varepsilon}_f^* \times \boldsymbol{\varepsilon}_i) \cdot \mathbf{m}(\mathbf{r})]}_{\text{Circular dichroism}},$$

where E is the energy, $\mathbf{r}$ is the position vector, $\boldsymbol{\varepsilon}_f$ and $\boldsymbol{\varepsilon}_i$ are the initial and final Jones polarization vectors, respectively, $f_c(E)$ is the electronic scattering factor, $f_1(E)$ is the magnetic scattering factor, and $\mathbf{m}(\mathbf{r})$ is the orientation of magnetization. For the case of circularly polarized light, the complex scattering factor reduces to

$$f(E, r) = \underbrace{f_c(E)}_{\text{Electronic}} \pm \underbrace{if_1(E)\mathbf{m}(\mathbf{r}) \cdot \hat{\mathbf{k}}}_{\text{Circular dichroism}},$$

where $\hat{\mathbf{k}}$ a unit vector representing the direction of propagation of x rays. Further details on the relationship between A and ϕ to the scattering factor is explained in Ref. [16]. Given that $A(E) \propto e^{\mathrm{Im}[f_1(E)]\mathbf{m}\cdot\hat{\mathbf{k}}}$, where $\mathrm{Im}[f_1(E)]$ is the imaginary part of the magnetic scattering factor, the logarithmic difference between RCP and LCP gives the pure magnetic scattering factor, and we define our A_{XMCD} signal as

$$A_{\mathrm{XMCD}} = \frac{\ln(A_{\mathrm{RCP}}) - \ln(A_{\mathrm{LCP}})}{2} \times 100$$
$$\propto \mathrm{Im}[f_1(E)]\mathbf{m} \cdot \hat{\mathbf{k}},$$

while the direct difference between the RCP and LCP phase images gives the ϕ_{XMCD} signal:

$$\phi_{\mathrm{XMCD}} = \phi_{\mathrm{RCP}} - \phi_{\mathrm{LCP}} \propto \mathrm{Re}[f_1(E)]\mathbf{m} \cdot \hat{\mathbf{k}},$$

where $\mathrm{Re}[f_1(E)]$ is the real part of the magnetic scattering factor.

APPENDIX B: SAMPLE FABRICATION

1. CoPt and FeGd multilayers

The 100 nm CoPt film is grown with the following composition $\mathrm{Ta}\backslash\mathrm{Pt}(4\,\mathrm{nm})\backslash\mathrm{Co}(1\,\mathrm{nm})\backslash\mathrm{Pt}(1\,\mathrm{nm}) \times 50\backslash\mathrm{Ru}(3\,\mathrm{nm})$ by magnetron sputtering on an x-ray transparent 5 mm × 5 mm silicon nitride ($\mathrm{Si_3N_4}$) membrane. The magnetic Fe:Gd (70:30 at.%) films of various thicknesses are deposited via magnetron cosputtering on 5 mm × 5 mm $\mathrm{Si_3N_4}$ windows at a base pressure of 1×10^{-8} Torr and Ar sputtering atmosphere pressure of 3 mTorr using a commercial sputtering system. Holes in the films are milled with a focused Ga ion beam to provide a region for alignment and normalization.

2. $\mathrm{Co_8Zn_9Mn_3}$ single crystal

The $\mathrm{Co_8Zn_9Mn_3}$ crystals are grown via the Bridgman method. Stoichiometric amounts of Co powder (Alfa-Aesar, 99.99%), Zn powder (SigmaAldrich, 99.995%), and Mn pieces (Alfa-Aesar, 99.99%) are ground together. The mixture is then transferred to an alumina crucible with a pointed end and vacuum sealed inside quartz tube. The sealed tube is then heated to 1060 °C and allowed to homogenize for 12 h. It is then slowly cooled at a rate of 1 °C/h to 700 °C and annealed for several days at the same temperature before being water quenched. Single crystals of $\mathrm{Co_8Zn_9Mn_3}$ are isolated from the as-grown boule and oriented using x-ray Laue backreflection [42]. Using a focused Ga ion beam, a lamella of $\mathrm{Co_8Zn_9Mn_3}$ is extracted with a lift-out method using an *in situ* micromanipulator. The lamella is milled into cylindrical shaped samples of thickness 900 nm thick, which is then transferred and positioned into an x-ray transparent 3 mm × 3 mm silicon nitride ($\mathrm{Si_3Ni_4}$) membrane using the *in situ* micromanipulator needle and fixed in place by depositing platinum on one corner of the sample.

3. Magnetite sample collection and preparation

The natural magnetite sample is extracted from southwest Pacific marine sediments drilled by the International Ocean Discovery Program (IODP), located at IODP site U1511B, section 32R1W, interval 80-81. The sediment is dissolved in water and processed to isolate magnetic fractions following the protocol of Ref. [57]. Magnetic extracts are deposited on a TEM copper grid for STEM imaging to locate the target magnetite particle. STEM imaging is conducted at the Wolfson Electron Microscopy Suite, University of Cambridge, using a FEI Krios TEM operating at 300 kV and 80 K.

APPENDIX C: PTYCHOGRAPHY SETUP AND RECONSTRUCTION

For each ptychography scan, diffraction patterns are recorded on a 2048×2048 pixel scientific complementary metal oxide semiconductor (sCMOS) area detector (AXIS-SXRF-2020EUV, Axis Photonique Inc.) with an exposure of 40 ms while laterally scanning the sample with a piezo scanner in a spiral pattern across the x-ray beam, to minimize grid pathology artifacts. The sCMOS camera with a pixel size of 6.5 μm is placed approximately 72 mm downstream of the sample. The sample is placed about 70 μm downstream of the focus formed by a Fresnel zone plate with a diameter of 333 μm, width of the outermost zone of 70 nm, and a mean focal length of 14.154 mm (for photon energy range 770–807 eV) and 12.835 mm (for 700–730 eV), producing a defocused beam with a full width at half maximum of approximately 1 μm. Together with a scanning step size of 200 nm, this gives a linear distance overlap ratio [58] of about 80%. The coherent flux incident on the sample has been estimated to about 10^{10} photons per second. For a ptychography scan consisting of 1924 points for a circular field of view of 8 μm radius, the total exposure time is 79.96 s. As a result, the accumulated photon incident on the sample per image, taking into account the size of the beam, is approximately 3.8×10^9 photons per μm^2. At the beginning of each scan, a single dark image is collected which is subtracted from all raw diffraction images of that scan. In addition, all raw images are losslessly reduced to a 512×512 image by first cropping the central 1024×1024 pixels and then binning the image by a factor of 2 along each dimension. The ptychographic reconstructions are performed using the PTYPY software [34], loading the clean dark-subtracted 512×512 diffraction images together with their corresponding scan positions as recorded by an interferometric system and subsequently running 1000 iterations of the graphical processing unit accelerated implementation of the difference map algorithm [59]. The CoPt spectroptychography images are reconstructed with a fixed pixel size of 17.414 nm, and FeGd spectroptychography images are reconstructed with a fixed pixel size of 11.162 nm, to account for the energy-dependent pixel size of the dichroic spectroptychography scans. This is done in PTYPY by cropping or padding the forward and backward propagators accordingly. This value corresponds to the pixel size of the ptychographic reconstruction associated with the lowest photon energy. The scans of the $Co_8Zn_9Mn_3$ and the natural magnetite particles are acquired with the same setup but with a sCMOS camera of pixel size 11 μm. The ptychography scans of the $Co_8Zn_9Mn_3$ chiral magnet is reconstructed by running 1000 iterations of the relaxed average alternating reflection algorithm [60] as implemented in PTYPY [34]. The pixel size of the reconstructions is 10.173 nm. The ptychography scans of the natural magnetite particles are reconstructed by running 1000 iterations of the difference map algorithm. The pixel size of the reconstructions is 11.16 nm.

APPENDIX D: IMAGE ANALYSIS

The analysis is carried out using PYTHON3.9.16 in a Jupyter Lab environment [61–64]. The images undergo a preprocessing routine to quantitatively extract the magnetic contrast. All images are aligned with respect to a feature in the image, for example, for the case of the films, a hole on the sample [shown in Fig. 2(b)], and all phase projections are corrected for a linear phase ramp [65]. Additionally, to filter low-frequency noise from the phase images, a Gaussian filter with high sigma is applied to blur the phase image, which is then subsequently subtracted from the respective unfiltered phase image. In order to normalize with respect to the incident beam, all amplitude images are divided by the average value inside the hole, whereas an offset phase found within the hole is subtracted from all phase images. Once images are normalized, they are aligned with respect to each other with a subpixel image registration algorithm [66] as implemented in Ref. [63]. For A_{XMCD} images, the logarithm of the amplitude images is taken and then the difference between RCP (A_{RCP}) and LCP (A_{LCP}) is taken to subtract the electronic scattering factor. Similarly for the ϕ_{XMCD} images, the difference between RCP and LCP is taken to subtract the electronic contribution to the scattering factor. The equations are as follows:

$$A_{\mathrm{XMCD}} = \frac{\ln(A_{\mathrm{RCP}}) - \ln(A_{\mathrm{LCP}})}{2} \times 100,$$

$$\phi_{\mathrm{XMCD}} = \frac{\phi_{\mathrm{RCP}} - \phi_{\mathrm{LCP}}}{2}.$$

Quantitative data are extracted from the projections as follows. The transmission as a function of energy is obtained by taking the square of the absolute value of the complex images taken at each energy, averaging over both positive and negative domains [plotted as a black line in Fig. 3(b)]. We observe two resonance peaks corresponding to the L_3 and L_2 absorption edges of cobalt. In order to quantitatively extract the complex XMCD spectra from the images, we average the XMCD signal within each domain and obtain the spectra shown in Fig. 3(b) for both A_{XMCD} (red curve) and ϕ_{XMCD} (blue curve). This is done by generating a boolean mask for the domains by running a Chan Vese segmentation algorithm [67] as implemented in Ref. [63], on a high-SNR A_{XMCD} image taken on-resonance at 780 eV. This gives two masks, one for each domain. These masks are then applied to the whole stack of aligned images to extract the magnetic signal from the same regions. The area taken from each image at each energy is then averaged to produce the quantitative spectra shown in Fig. 3(b).

APPENDIX E: SIMULATION OF THICKER SAMPLES

To determine the SNR of the A_{XMCD} and ϕ_{XMCD} images as a function of thickness, we separately determine the thickness evolution of the signal, noise, and then the calculation of the SNR.

1. Signal

In order to simulate the transmission intensity for thicker samples, we calculate the absorption coefficient of the material with the measured transmission spectra [black curve in Fig. 3(b)], from $I = e^{-\mu_{\mathrm{abs}} z}$, where I is the transmitted intensity through the sample [$I = A(E)^2$ with $A(E)$ being the normalized measured amplitude], μ_{abs} is the absorption coefficient, and z is the thickness of the material. Now, using this same equation, we can calculate the transmitted intensity as a function of energy for different thicknesses of a particular material, as shown in Fig. 4(a).

To simulate the A_{XMCD} spectra for different thicknesses, we first calculate the transmission intensity from the dichroic spectroptychography projections taken with both RCP (I_{RCB}) and LCP (I_{LCP}) x rays. We then separately obtain the absorption coefficients $\mu_{\mathrm{RCP(LCP)}} \propto \mathrm{Im}[f(E, r)]$, assuming the magnetization vector is oriented (anti)parallel to the direction of propagation of x rays, similar to the measurements. Now using $I_{\mathrm{RCP(LCP)}} = e^{-\mu_{\mathrm{RCP(LCP)}} z}$, we calculate the transmission for various thickness for RCP (I_{RCB}) and LCP (I_{LCP}) x rays. To isolate the A_{XMCD} signal, we use the following equation:

$$A_{\mathrm{XMCD}} = \frac{\ln(I_{\mathrm{RCP}}) - \ln(I_{\mathrm{LCP}})}{4} \times 100, \tag{E1}$$

where the factor of 4 accounts for the transformation from intensity to amplitude. Additionally, to impose the constraint of transmission dropping to zero after a certain thickness, we set the value to zero below a certain threshold transmission of 0.05% of the total transmission.

Similarly given that $\phi = \delta z$, with $\delta \propto \mathrm{Re}[f(E, r)]$, assuming the magnetization vector is oriented (anti)parallel to the direction of propagation of x rays, similar to the measurements, we calculate δ from the measured dichroic

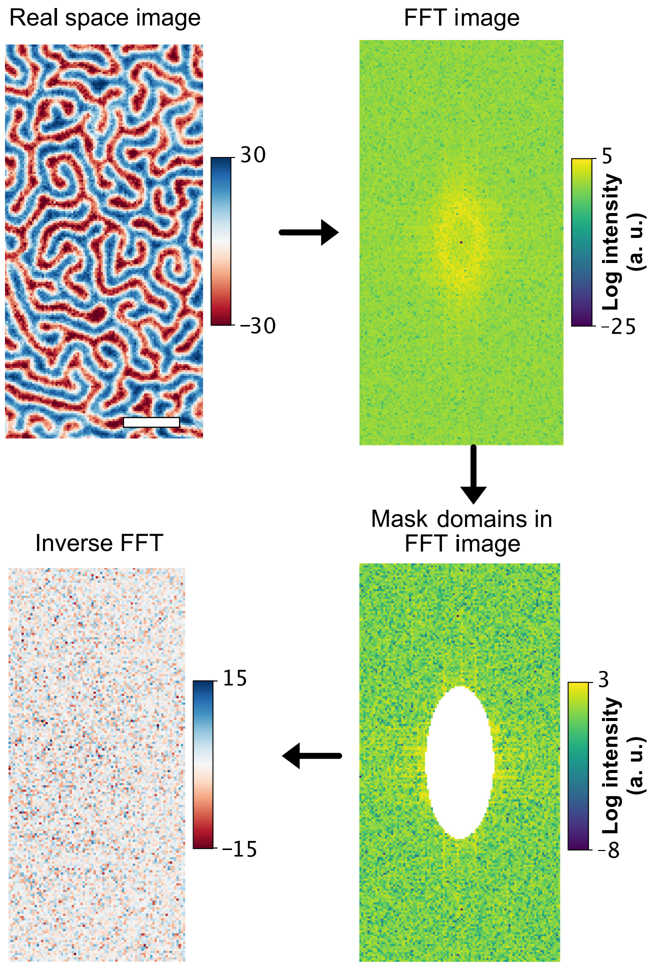

FIG. 8. Protocol used for extracting noise in measurement data. The scale bar in the real space image (top left) represents 500 nm.

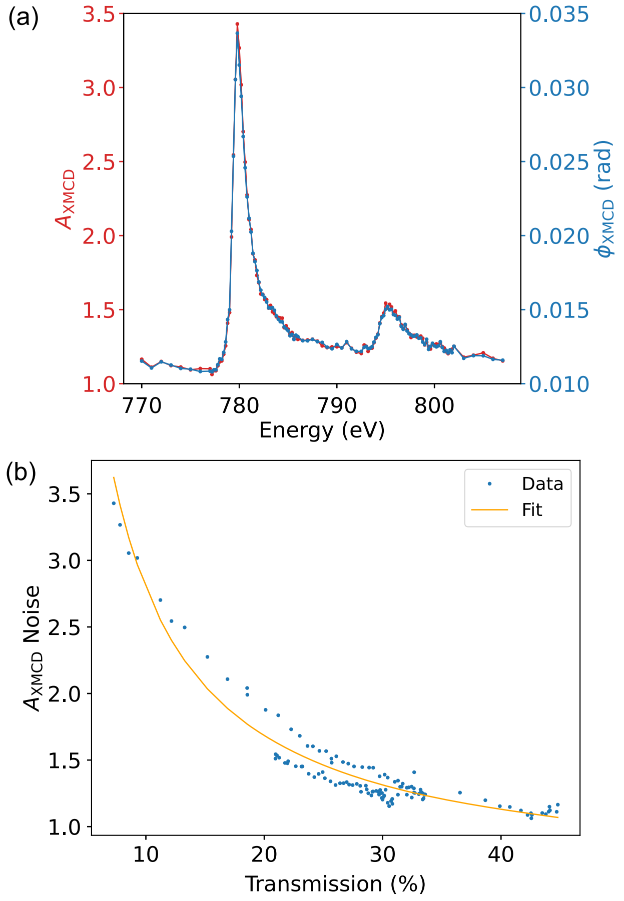

FIG. 9. (a) A_{XMCD} and ϕ_{XMCD} noise as a function of energy for 100 nm CoPt. The noise increases as we approach resonance as transmission decreases. (b) A_{XMCD} noise as a function of transmission. The fit has a $1/x$ dependence, which is used to calculate the noise for lower transmission corresponding to transmission through thicker samples. A similar fit is done for the ϕ_{XMCD} noise.

phase spectra taken with RCP (ϕ_{RCP}) and LCP (ϕ_{LCP}) x rays. Using the same equation, we then simulate the ϕ_{RCP} and ϕ_{LCP} spectra for thicker samples and the ϕ_{XMCD} obtained for each thickness using the following equation:

$$\phi_{\mathrm{XMCD}} = \frac{\phi_{\mathrm{RCP}} - \phi_{\mathrm{LCP}}}{2}.$$

2. Noise

The noise is calculated differently for the thin and thick regime. We first consider the thin regime, where the noise of the images for the 100 nm CoPt and 400 nm FeGd is calculated by taking the standard deviation of the high-frequency noise present in the system. This was done by performing a fast Fourier transform (FFT) of an XMCD image and masking the frequency regime corresponding to the domains. We then perform an inverse FFT and take the standard deviation of the filtered image. An example is shown in Fig. 8. The value of the noise as a function of energy is given in Fig. 9(a): As the transmission decreases, the noise increases. It can be seen that, although the A_{XMCD} (dimensionless) and ϕ_{XMCD} (rad) are two different quantities, the noise as a function of energy is very similar. This is because both quantities are retrieved from the same diffraction patterns that are measured by the detector, and, thus, the noise of the ptychography projections can be directly related to the intensity on the detector.

For the thick regime with the 1- and 1.7-μm-thick FeGd, the noise also includes modulated noise within the domains, due to contrast present only in the vicinity of the domain walls. Hence, in order to calculate the noise for the images of 1- and 1.7-μm-thick FeGd, the average of the standard deviation of the XMCD signal seen within each domain gives the A_{XMCD} and ϕ_{XMCD} noise in the images.

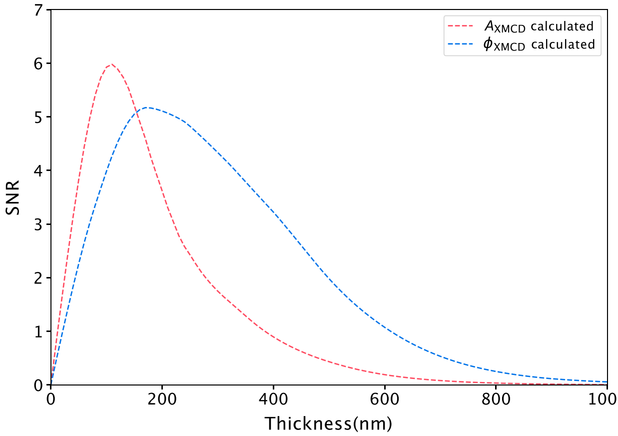

FIG. 10. Simulated SNR of A_{XMCD} and ϕ_{XMCD}. The ϕ_{XMCD} SNR is higher for increasing thickness than the A_{XMCD}. This plot is scaled in thickness for FeGd, for a direct comparison with experimental data, shown in Fig. 5(b).

3. Calculation of SNR

Having obtained the noise from the images, we calculate the dimensionless SNR for each sample separately using the respective signal obtained from measurements. The maximum SNR value for each of the samples is then taken and plotted as a function of thickness for all measured samples, shown in Fig. 5(b) as red and blue dots for the A_{XMCD} and ϕ_{XMCD}, respectively.

To determine the noise for the simulated data, we first obtain a relation between the measured noise and transmission, by plotting the noise as a function of transmission in Fig. 9(b), where we see a $1/x$ dependence in the noise. Using this relation, we calculate the noise we expect to see for thicker samples and calculate the SNR for the simulated data for CoPt, which is plotted as dashed lines in Fig. 10.

In order to compare the simulated CoPt SNR curves with measured FeGd, we arbitrarily scale the thickness of both simulated SNR curves to match the experimental data as shown in Fig. 5(b). This calculation of the dimensionless SNR allows us to compare the quality of the images originating from the two contrast mechanisms.

The thickness of 100-nm-thick CoPt is matched to an effective thickness of 217-nm-thick FeGd by comparing and scaling the measured transmission spectra between 100-nm-thick CoPt and 400-nm-thick FeGd. The main difference between the two arises from the different scattering factor, i.e., absorption coefficient μ. Although resonance occurs at different energies, by comparing both measured transmission spectra, we can estimate a scaling factor of 1.45 to effectively match the transmission of the

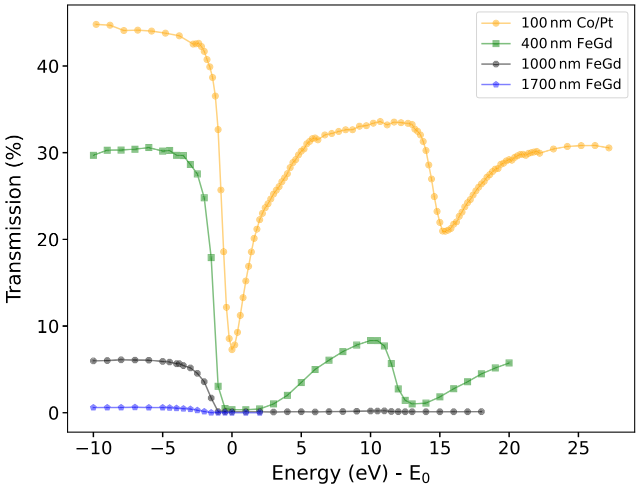

FIG. 11. Transmission signal through the thickness of the 100-nm-thick CoPt multilayer (yellow), 400 nm (green), 1 μm (black), and 1.7 μm (blue) FeGd samples. The energies are normalized with respect to the L_3 absorption edge of the materials at 780 eV for Co and 710 eV for Fe. Nonzero transmission is measurable only at preabsorption edges for the thick FeGd samples. On-resonance, the transmission is zero.

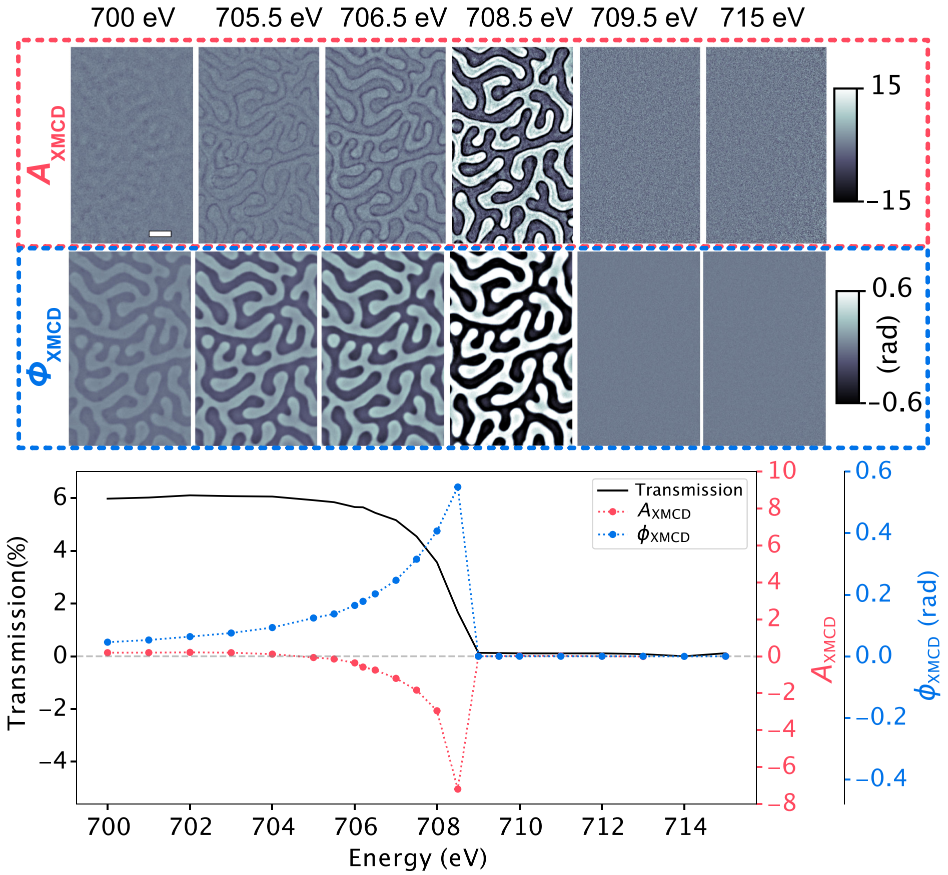

FIG. 12. Pre-edge phase ptychography on 1-μm-thick FeGd samples close to the Fe L_3 edge. Complex XMCD spectrum across the Fe L_3 edge extracted from magnetic domains in XMCD projections of a 1-μm-thick FeGd film with A_{XMCD} and ϕ_{XMCD} shown as red and blue dots, respectively. The black line indicates the transmission through the sample. The images above the plot show A_{XMCD} and ϕ_{XMCD} images for a few selections of energies. The scale bar represents 500 nm.

two samples to yield an effective thickness with respect to each other.

APPENDIX F: SPECTROPTYCHOGRAPHY ON FeGd SAMPLES

We performed spectroptychography scans on FeGd samples of thicknesses 400 nm, 1 μm, and 1.7 μm across the L_3 and L_2 edges of Fe. The transmission of the samples, plotted in Fig. 11, decreases dramatically on-resonance, with no transmission at the Fe L_3 absorption edge (normalized to zero energy) for all FeGd samples. However, even for the 1.7 μm-thick film, there remains detectable transmission in the pre-edge. By exploiting the ϕ_{XMCD} in the preabsorption edge, we are successfully able to image FeGd samples up to 1.7 μm with high contrast and nanoscale spatial resolution. The complex XMCD spectra, along with a selection of A_{XMCD} and ϕ_{XMCD} projections, are given for the 1-μm-thick film in Fig. 12.

APPENDIX G: SPATIAL RESOLUTION

The full-period spatial resolution of the images with the strongest XMCD contrast are calculated by Fourier ring correlation (FRC) with a half bit threshold [68] as implemented in Ref. [69]. An example is shown in Fig. 13, and the values observed for the different thickness are summarized in Table I.

In comparison, the ϕ_{XMCD}, in general, exhibits a slightly higher spatial resolution calculated with the FRC in comparison with the A_{XMCD}. Although ultrahigh nanoscale spatial resolutions are possible to measure with ptychography, they are not achieved here, as it was not the goal of the experiment. Rather than devoting the statistics to high spatial resolution, the limited beam

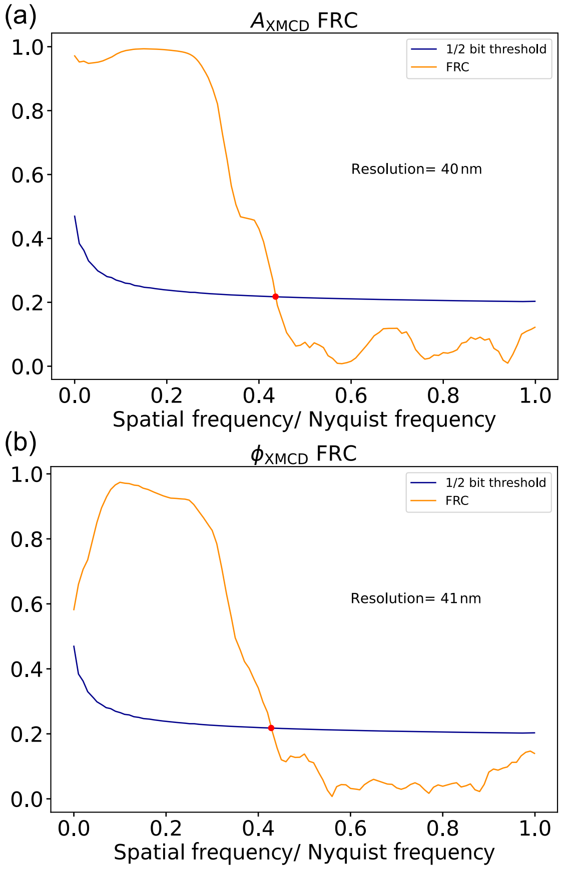

FIG. 13. Fourier ring correlation with half bit threshold for 100-nm-thick CoPt on (a) A_{XMCD} image taken at 780.0 eV and (b) ϕ_{XMCD} image taken at 779.4 eV.

time awarded was devoted instead to measuring the various samples with high energy resolution. In order to obtain higher spatial resolutions, the experiment could be further optimized, acquiring a larger portion of the detector, and acquiring higher statistics to further reduce the noise in the images. The spatial resolution obtained with FRC is relatively similar for the ϕ_{XMCD} and A_{XMCD} with the ϕ_{XMCD} offering a slightly higher resolution. The main difference between the A_{XMCD} and the ϕ_{XMCD} can be seen in the SNR of the images, with the ϕ_{XMCD} typically offering higher quality for thicker systems.

TABLE I. Summary of the spatial resolution by FRC with a half bit threshold. The phase has a higher spatial resolution than the amplitude for thicker samples.

	FRC (nm)	
Thickness (nm)	Amplitude	Phase
100 CoPt	40	41
400 FeGd	55	48
1000 FeGd	52	47
1700 FeGd	57	56

APPENDIX H: MICROMAGNETIC SIMULATIONS

Simulations of the $Co_8Zn_9Mn_3$ states are performed using the micromagnetic finite difference code OOMMF, within the UBERMAG simulation package [70]. The system is described by the archetypal energy functional, where m is the normalized magnetization field, A is the exchange constant, D is the bulk DMI constant, Ms is the saturation magnetization, B is the applied field, and Bd is the demagnetizing field. The exchange and DMI constants utilized are $A = 5.729 \times 10^{-12}$ J/m and $D = 0.55 \times 10^{-3}$ J/m^2, respectively, following the approach of Birch *et al.* [42]. A saturation magnetization of $Ms = 4.6055 \times 10^5$ A/m is used. The applied magnetic field is set to zero. The (confined region) is simulated using a rectangular region with dimensions $2 \times 2 \times 0.9$ μm, which is discretized using cubic cells of 10 nm edge length. The cylinder is simulated using a cylindrical region with height 0.9 μm and diameter 2 μm, which is discretized using cubic cells of 10 nm edge length. Systems are initialized with a random initial magnetization configuration and relaxed using a gradient descent method.

[1] J. L. Kirschvink, M. M. Walker, and C. E. Diebel, *Magnetite-based magnetoreception*, Curr. Opin. Neurobiol. **11**, 462 (2001).
[2] P. Robinson, R. J. Harrison, S. A. McEnroe, and R. B. Hargraves, *Lamellar magnetism in the haematite-ilmenite series as an explanation for strong remanent magnetization*, Nature (London) **418**, 517 (2002).
[3] O. Gutfleisch, M. A. Willard, E. Brück, C. H. Chen, S. G. Sankar, and J. P. Liu, *Magnetic materials and devices for the 21st century: Stronger, lighter, and more energy efficient*, Adv. Mater. **23**, 821 (2011).
[4] Y. Jiang, S. Masaoka, T. Fujita, M. Uehara, T. Toyonaga, K. Fujii, K. Higuchi, and K. Maenaka, *Fabrication of a vibration-driven electromagnetic energy harvester with integrated* NdFeB/Ta *multilayered micro-magnets*, J. Micromech. Microeng. **21**, 095014 (2011).
[5] S. Sugimoto, *Current status and recent topics of rare-earth permanent magnets*, J. Phys. D **44**, 064001 (2011).
[6] R. Dee and J. Cates, *Advanced MR read/inductive write heads for high performance, high density tape applications*, IEEE Trans. Magn. **34**, 1866 (1998).
[7] S. S. P. Parkin, M. Hayashi, and L. Thomas, *Magnetic domain-wall racetrack memory*, Science **320**, 190 (2008).
[8] A. Fert, V. Cros, and J. Sampaio, *Skyrmions on the track*, Nat. Nanotechnol. **8**, 152 (2013).
[9] M. Takeuchi, M. Suzuki, S. Kobayashi, Y. Kotani, T. Nakamura, N. Kikuchi, A. Bolyachkin, H. Sepehri-Amin, T. Ohkubo, K. Hono, Y. Une, and S. Okamoto, *Real picture of magnetic domain dynamics along the magnetic hysteresis curve inside an advanced permanent magnet*, NPG Asia Mater. **14**, 70 (2022).
[10] W. Jiang, P. Upadhyaya, W. Zhang, G. Yu, M. B. Jungfleisch, F. Y. Fradin, J. E. Pearson, Y. Tserkovnyak, K. L. Wang, O. Heinonen, S. G. E. te Velthuis, and

A. Hoffmann, *Blowing magnetic skyrmion bubbles*, Science **349**, 283 (2015).

[11] K. M. Song, J.-S. Jeong, B. Pan, X. Zhang, J. Xia, S. Cha, T.-E. Park, K. Kim, S. Finizio, J. Raabe, J. Chang, Y. Zhou, W. Zhao, W. Kang, H. Ju, and S. Woo, *Skyrmion-based artificial synapses for neuromorphic computing*, Natl. Electron. Rev. **3**, 148 (2020).

[12] W. Chao, P. Fischer, T. Tyliszczak, S. Rekawa, E. Anderson, and P. Naulleau, *Real space soft x-ray imaging at 10 nm spatial resolution*, Opt. Express **20**, 9777 (2012).

[13] A. Hierro-Rodriguez, C. Quirós, A. Sorrentino, L. M. Alvarez-Prado, J. I. Martín, J. M. Alameda, S. McVitie, E. Pereiro, M. Vélez, and S. Ferrer, *Revealing 3d magnetization of thin films with soft x-ray tomography: Magnetic singularities and topological charges*, Nat. Commun. **11**, 6382 (2020).

[14] C. Phatak, A. Petford-Long, and M. De Graef, *Recent advances in Lorentz microscopy*, Curr. Opin. Solid State Mater. Sci. **20**, 107 (2016).

[15] D. Wolf, S. Schneider, U. K. Rößler, A. Kovács, M. Schmidt, R. E. Dunin-Borkowski, B. Büchner, B. Rellinghaus, and A. Lubk, *Unveiling the three-dimensional magnetic texture of skyrmion tubes*, Nat. Nanotechnol. **17**, 250 (2022).

[16] C. Donnelly, V. Scagnoli, M. Guizar-Sicairos, M. Holler, F. Wilhelm, F. Guillou, A. Rogalev, C. Detlefs, A. Menzel, J. Raabe, and L. J. Heyderman, *High-resolution hard x-ray magnetic imaging with dichroic ptychography*, Phys. Rev. B **94**, 064421 (2016).

[17] C. Donnelly, M. Guizar-Sicairos, V. Scagnoli, S. Gliga, M. Holler, J. Raabe, and L. J. Heyderman, *Three-dimensional magnetization structures revealed with x-ray vector nanotomography*, Nature (London) **547**, 328 (2017).

[18] C. Donnelly, K. L. Metlov, V. Scagnoli, M. Guizar-Sicairos, M. Holler, N. S. Bingham, J. Raabe, L. J. Heyderman, N. R. Cooper, and S. Gliga, *Experimental observation of vortex rings in a bulk magnet*, Nat. Phys. **17**, 316 (2021).

[19] C. Donnelly, S. Finizio, S. Gliga, M. Holler, A. Hrabec, M. Odstrčil, S. Mayr, V. Scagnoli, L. J. Heyderman, M. Guizar-Sicairos, and J. Raabe, *Time-resolved imaging of three-dimensional nanoscale magnetization dynamics*, Nat. Nanotechnol. **15**, 356 (2020).

[20] S. Seki, M. Suzuki, M. Ishibashi, R. Takagi, N. D. Khanh, Y. Shiota, K. Shibata, W. Koshibae, Y. Tokura, and T. Ono, *Direct visualization of the three-dimensional shape of skyrmion strings in a noncentrosymmetric magnet*, Nat. Mater. **21**, 181 (2022).

[21] J. Miao, P. Charalambous, J. Kirz, and D. Sayre, *Extending the methodology of x-ray crystallography to allow imaging of micrometre-sized non-crystalline specimens*, Nature (London) **400**, 342 (1999).

[22] Y. Tokunaga, X. Z. Yu, J. S. White, H. M. Rønnow, D. Morikawa, Y. Taguchi, and Y. Tokura, *A new class of chiral materials hosting magnetic skyrmions beyond room temperature*, Nat. Commun. **6**, 7638 (2015).

[23] M. Blume and D. Gibbs, *Polarization dependence of magnetic x-ray scattering*, Phys. Rev. B **37**, 1779 (1988).

[24] B. T. Thole, P. Carra, F. Sette, and G. van der Laan, *X-ray circular dichroism as a probe of orbital magnetization*, Phys. Rev. Lett. **68**, 1943 (1992).

[25] P. Carra, B. T. Thole, M. Altarelli, and X. Wang, *X-ray circular dichroism and local magnetic fields*, Phys. Rev. Lett. **70**, 694 (1993).

[26] J. R. Fienup, *Phase retrieval algorithms: A comparison*, Appl. Opt. **21**, 2758 (1982).

[27] F. Pfeiffer, M. Bech, O. Bunk, T. Donath, B. Henrich, P. Kraft, and C. David, *X-ray dark-field and phase-contrast imaging using a grating interferometer*, J. Appl. Phys. **105**, 102006 (2009).

[28] K. A. Nugent, A. G. Peele, H. N. Chapman, and A. P. Mancuso, *Unique phase recovery for nonperiodic objects*, Phys. Rev. Lett. **91**, 203902 (2003).

[29] A. Scherz, W. F. Schlotter, K. Chen, R. Rick, J. Stöhr, J. Lüning, I. McNulty, C. Günther, F. Radu, W. Eberhardt, O. Hellwig, and S. Eisebitt, *Phase imaging of magnetic nanostructures using resonant soft x-ray holography*, Phys. Rev. B **76**, 214410 (2007).

[30] X. Shi, P. Fischer, V. Neu, D. Elefant, J. C. T. Lee, D. A. Shapiro, M. Farmand, T. Tyliszczak, H. W. Shiu, S. Marchesini, S. Roy, and S. D. Kevan, *Soft x-ray ptychography studies of nanoscale magnetic and structural correlations in thin* $\mathrm{SmCo_5}$ *films*, Appl. Phys. Lett. **108**, 094103 (2016).

[31] X. Zhu, A. P. Hitchcock, D. A. Bazylinski, P. Denes, J. Joseph, U. Lins, S. Marchesini, H.-W. Shiu, T. Tyliszczak, and D. A. Shapiro, *Measuring spectroscopy and magnetism of extracted and intracellular magnetosomes using soft x-ray ptychography*, Proc. Natl. Acad. Sci. U.S.A. **113**, E8219 (2016).

[32] Y. H. Lo, J. Zhou, A. Rana, D. Morrill, C. Gentry, B. Enders, Y.-S. Yu, C.-Y. Sun, D. A. Shapiro, R. W. Falcone, H. C. Kapteyn, M. M. Murnane, P. U. P. A. Gilbert, and J. Miao, *X-ray linear dichroic ptychography*, Proc. Natl. Acad. Sci. U.S.A. **118**, e2019068118 (2021).

[33] M. Guizar-Sicairos and P. Thibault, *Ptychography: A solution to the phase problem*, Phys. Today **74**, No. 9, 42 (2021).

[34] B. Enders and P. Thibault, *A computational framework for ptychographic reconstructions*, Proc. R. Soc. A **472**, 20160640 (2016).

[35] M. T. Birch, D. Cortés-Ortuño, L. A. Turnbull, M. N. Wilson, F. Groß, N. Träger, A. Laurenson, N. Bukin, S. H. Moody, M. Weigand, G. Schütz, H. Popescu, R. Fan, P. Steadman, J. A. T. Verezhak, G. Balakrishnan, J. C. Loudon, A. C. Twitchett-Harrison, O. Hovorka, H. Fangohr, F. Y. Ogrin, J. Gräfe, and P. D. Hatton, *Real-space imaging of confined magnetic skyrmion tubes*, Nat. Commun. **11**, 1726 (2020).

[36] P. Milde, D. Köhler, J. Seidel, L. M. Eng, A. Bauer, A. Chacon, J. Kindervater, S. Mühlbauer, C. Pfleiderer, S. Buhrandt, C. Schütte, and A. Rosch, *Unwinding of a skyrmion lattice by magnetic monopoles*, Science **340**, 1076 (2013).

[37] F. Zheng, F. N. Rybakov, A. B. Borisov, D. Song, S. Wang, Z.-A. Li, H. Du, N. S. Kiselev, J. Caron, A. Kovács, M. Tian, Y. Zhang, S. Blügel, and R. E. Dunin-Borkowski, *Experimental observation of chiral magnetic bobbers in B20-type* FeGe, Nat. Nanotechnol. **13**, 451 (2018).

[38] F. N. Rybakov, N. S. Kiselev, A. B. Borisov, L. Döring, C. Melcher, and S. Blügel, *Magnetic hopfions in solids*, APL Mater. **10**, 111113 (2022).

[39] X. Yu, Y. Liu, K. V. Iakoubovskii, K. Nakajima, N. Kanazawa, N. Nagaosa, and Y. Tokura, *Realization and current-driven dynamics of fractional hopfions and their ensembles in a helimagnet* FeGe, Adv. Mater. **35**, 2210646 (2023).

[40] N. Kent, N. Reynolds, D. Raftrey, I. T. G. Campbell, S. Virasawmy, S. Dhuey, R. V. Chopdekar, A. Hierro-Rodriguez, A. Sorrentino, E. Pereiro, S. Ferrer, F. Hellman, P. Sutcliffe, and P. Fischer, *Creation and observation of hopfions in magnetic multilayer systems*, Nat. Commun. **12**, 1562 (2021).

[41] F. Zheng, N. S. Kiselev, F. N. Rybakov, L. Yang, W. Shi, S. Blügel, and R. E. Dunin-Borkowski, *Hopfion rings in a cubic chiral magnet*, Nature (London) **623**, 718 (2023).

[42] M. T. Birch, D. Cortés-Ortuño, K. Litzius, S. Wintz, F. Schulz, M. Weigand, A. Štefančič, D. A. Mayoh, G. Balakrishnan, P. D. Hatton, and G. Schütz, *Toggle-like current-induced Bloch point dynamics of 3d skyrmion strings in a room temperature nanowire*, Nat. Commun. **13**, 3630 (2022).

[43] C. Donnelly and V. Scagnoli, *Imaging three-dimensional magnetic systems with x-rays*, J. Phys. Condens. Matter **32**, 213001 (2020).

[44] S. Seki, M. Suzuki, M. Ishibashi, R. Takagi, N. D. Khanh, Y. Shiota, K. Shibata, W. Koshibae, Y. Tokura, and T. Ono, *Direct visualization of the three-dimensional shape of skyrmion strings in a noncentrosymmetric magnet*, Nat. Mater. **21**, 181 (2022).

[45] A. Rana, C.-T. Liao, E. Iacocca, J. Zou, M. Pham, X. Lu, E.-E. C. Subramanian, Y. H. Lo, S. A. Ryan, C. S. Bevis, R. M. Karl, A. J. Glaid, J. Rable, P. Mahale, J. Hirst, T. Ostler, W. Liu, C. M. O'Leary, Y.-S. Yu, K. Bustillo, H. Ohldag, D. A. Shapiro, S. Yazdi, T. E. Mallouk, S. J. Osher, H. C. Kapteyn, V. H. Crespi, J. V. Badding, Y. Tserkovnyak, M. M. Murnane, and J. Miao, *Three-dimensional topological magnetic monopoles and their interactions in a ferromagnetic meta-lattice*, Nat. Nanotechnol. **18**, 227 (2023).

[46] M. Di Pietro Martínez, A. Wartelle, C. Herrero Martínez, F. Fettar, F. Blondelle, J.-F. Motte, C. Donnelly, L. Turnbull, F. Ogrin, G. van der Laan, H. Popescu, N. Jaouen, F. Yakhou-Harris, and G. Beutier, *Three-dimensional tomographic imaging of the magnetization vector field using Fourier transform holography*, Phys. Rev. B **107**, 094425 (2023).

[47] L. Chang, A. P. Roberts, W. Williams, J. D. Fitz Gerald, J. C. Larrasoaña, L. Jovane, and A. R. Muxworthy, *Giant magnetofossils and hyperthermal events*, Earth Planet. Sci. Lett. **351–352**, 258 (2012).

[48] P. Xue, L. Chang, Z. Pei, and R. J. Harrison, *Discovery of giant magnetofossils within and outside of the palaeocene-eocene thermal maximum in the North Atlantic*, Earth Planet. Sci. Lett. **584**, 117417 (2022).

[49] Y. Kimura, T. Kato, T. Tanigaki, T. Akashi, H. Kasai, S. Anada, R. Yoshida, K. Yamamoto, T. Nakamura, M. Sato, K. Amano, M. Kikuiri, T. Morita, E. Kagawa, T. Yada, M. Nishimura, A. Nakato, A. Miyazaki, K. Yogata, M. Abe, T. Okada, T. Usui, M. Yoshikawa, T. Saiki, S. Tanaka, F. Terui, S. Nakazawa, H. Yurimoto, T. Noguchi, R. Okazaki, H. Yabuta, H. Naraoka, K. Sakamoto, S.-i. Watanabe, Y. Tsuda, and S. Tachibana, *Visualization of nanoscale magnetic domain states in the asteroid Ryugu*, Sci. Rep. **13**, 14096 (2023).

[50] A. P. Roberts, T. P. Almeida, N. S. Church, R. J. Harrison, D. Heslop, Y. Li, J. Li, A. R. Muxworthy, W. Williams, and X. Zhao, *Resolving the origin of pseudo-single domain magnetic behavior*, J. Geophys. Res. **122**, 9534 (2017).

[51] I. Lascu, J. F. Einsle, M. R. Ball, and R. J. Harrison, *The vortex state in geologic materials: A micromagnetic perspective*, J. Geophys. Res. **123**, 7285 (2018).

[52] C. Donnelly, S. Gliga, V. Scagnoli, M. Holler, J. Raabe, L. J. Heyderman, and M. Guizar-Sicairos, *Tomographic reconstruction of a three-dimensional magnetization vector field*, New J. Phys. **20**, 083009 (2018).

[53] D. Schumann, T. D. Raub, R. E. Kopp, J.-L. Guerquin-Kern, T.-D. Wu, I. Rouiller, A. V. Smirnov, S. K. Sears, U. Lücken, S. M. Tikoo, R. Hesse, J. L. Kirschvink, and H. Vali, *Gigantism in unique biogenic magnetite at the paleocene-eocene thermal maximum*, Proc. Natl. Acad. Sci. U.S.A. **105**, 17648 (2008).

[54] J. F. J. Bryson, C. I. O. Nichols, J. Herrero-Albillos, F. Kronast, T. Kasama, H. Alimadadi, G. van der Laan, F. Nimmo, and R. J. Harrison, *Long-lived magnetism from solidification-driven convection on the pallasite parent body*, Nature (London) **517**, 472 (2015).

[55] J. Cui, M. Kramer, L. Zhou, F. Liu, A. Gabay, G. Hadjipanayis, B. Balasubramanian, and D. Sellmyer, *Current progress and future challenges in rare-earth-free permanent magnets*, Acta Mater. **158**, 118 (2018).

[56] 10.5281/zenodo.13306179

[57] P. Xue and L. Chang, *Spatiotemporal distribution of giant magnetofossils holds clues to their biological origin*, Geology **52**, 453 (2024).

[58] O. Bunk, M. Dierolf, S. Kynde, I. Johnson, O. Marti, and F. Pfeiffer, *Influence of the overlap parameter on the convergence of the ptychographical iterative engine*, Ultramicroscopy **108**, 481 (2008).

[59] V. Elser, *Phase retrieval by iterated projections*, J. Opt. Soc. Am. A **20**, 40 (2003).

[60] D. R. Luke, *Relaxed averaged alternating reflections for diffraction imaging*, Inverse Probl. **21**, 37 (2005).

[61] C. R. Harris, K. J. Millman, S. J. van der Walt, R. Gommers, P. Virtanen, D. Cournapeau, E. Wieser, J. Taylor, S. Berg, N. J. Smith, R. Kern, M. Picus, S. Hoyer, M. H. van Kerkwijk, M. Brett, A. Haldane, J. F. del Río, M. Wiebe, P. Peterson, P. Gérard-Marchant, K. Sheppard, T. Reddy, W. Weckesser, H. Abbasi, C. Gohlke, and T. E. Oliphant, *Array programming with numpy*, Nature (London) **585**, 357 (2020).

[62] P. Virtanen, R. Gommers, T. E. Oliphant, M. Haberland, T. Reddy, D. Cournapeau, E. Burovski, P. Peterson, W. Weckesser, J. Bright, S. J. van der Walt, M. Brett, J. Wilson, K. J. Millman, N. Mayorov, A. R. J. Nelson, E. Jones, R. Kern, E. Larson, C. J. Carey, İ. Polat, Y. Feng, E. W. Moore, J. VanderPlas, D. Laxalde, J. Perktold, R. Cimrman, I. Henriksen, E. A. Quintero, C. R. Harris, A. M. Archibald, A. H. Ribeiro, F. Pedregosa, P. van Mulbregt, A. Vijaykumar, A. P. Bardelli, A. Rothberg, A. Hilboll, A. Kloeckner, A. Scopatz, A. Lee, A. Rokem, C. N. Woods, C. Fulton, C. Masson, C. Häggström, C. Fitzgerald, D. A. Nicholson, D. R. Hagen, D. V. Pasechnik, E. Olivetti, E. Martin, E. Wieser, F. Silva, F. Lenders, F. Wilhelm, G. Young, G. A. Price, G.-L.

Ingold, G. E. Allen, G. R. Lee, H. Audren, I. Probst, J. P. Dietrich, J. Silterra, J. T. Webber, J. Slavič, J. Nothman, J. Buchner, J. Kulick, J. L. Schönberger, J. de Miranda Cardoso, J. Reimer, J. Harrington, J. L. C. Rodríguez, J. Nunez-Iglesias, J. Kuczynski, K. Tritz, M. Thoma, M. Newville, M. Kümmerer, M. Bolingbroke, M. Tartre, M. Pak, N. J. Smith, N. Nowaczyk, N. Shebanov, O. Pavlyk, P. A. Brodtkorb, P. Lee, R. T. McGibbon, R. Feldbauer, S. Lewis, S. Tygier, S. Sievert, S. Vigna, S. Peterson, S. More, T. Pudlik, T. Oshima, T. J. Pingel, T. P. Robitaille, T. Spura, T. R. Jones, T. Cera, T. Leslie, T. Zito, T. Krauss, U. Upadhyay, Y. O. Halchenko, Y. Vázquez-Baeza, and S... Contributors, *SCIPY1.0: Fundamental algorithms for scientific computing in PYTHON*, Nat. Methods **17**, 261 (2020).

[63] S. van der Walt, J. L. Schönberger, J. Nunez-Iglesias, F. Boulogne, J. D. Warner, N. Yager, E. Gouillart, T. Yu, the scikit-image contributors, and S. Gomez, *scikit-image: Image processing in PYTHON*, PeerJ **2**, e453 (2014).

[64] J. D. Hunter, *Matplotlib: A 2d graphics environment*, Comput. Sci. Eng. **9**, 90 (2007).

[65] M. Guizar-Sicairos, A. Diaz, M. Holler, M. S. Lucas, A. Menzel, R. A. Wepf, and O. Bunk, *Phase tomography from x-ray coherent diffractive imaging projections*, Opt. Express **19**, 21345 (2011).

[66] M. Guizar-Sicairos, S. T. Thurman, and J. R. Fienup, *Efficient subpixel image registration algorithms*, Opt. Lett. **33**, 156 (2008).

[67] *Scale-Space Theories in Computer Vision*, edited by M. Nielsen, P. Johansen, O. F. Olsen, and J. Weickert (Springer, Berlin, 1999).

[68] M. van Heel and M. Schatz, *Fourier shell correlation threshold criteria*, J. Struct. Biol. **151**, 250 (2005).

[69] V. Favre-Nicolin, G. Girard, S. Leake, J. Carnis, Y. Chushkin, J. Kieffer, P. Paleo, and M.-I. Richard, *PyNX: High-performance computing toolkit for coherent x-ray imaging based on operators*, J. Appl. Crystallogr. **53**, 1404 (2020).

[70] M. Beg, M. Lang, and H. Fangohr, *Ubermag: Towards more effective micromagnetic workflows*, IEEE Trans. Magn. **58**, 1 (2022).